Holocene thermokarst and pingo development in the Kolyma Lowland (NE Siberia)

Article (Accepted Version)

Holocene thermokarst and pingo development in the Kolyma Lowland (NE Siberia)

Sebastian Wetterich[1]*, Lutz Schirrmeister[1], Larisa Nazarova[1,2,3], Olga Palagushkina[2], Anatoly Bobrov[4], Lilit Pogosyan[5], Larisa Savelieva[6], Liudmila Syrykh[7,8], Heidrun Matthes[1], Michael Fritz[1], Frank Günther[1], Thomas Opel[9,1], Hanno Meyer[1]

[1]Alfred Wegener Institute Helmholtz Centre for Polar and Marine Research, Potsdam, Germany

[2]Kazan Federal University, Kazan, Russia

[3]University of Potsdam, Institute of Earth and Environmental Science, Potsdam, Germany

[4]Lomonosov Moscow State University, Faculty of Soil Science, Moscow, Russia

[5]Universidad Autónoma de México, Instituto de Geología, Posgrado en Ciencias de la Tierra, Ciudad de México, Mexico

[6]St. Petersburg State University, Institute of Earth Sciences, St. Petersburg, Russia

[7]Herzen State Pedagogical University, Institute of Geography, St. Petersburg, Russia

[8]Russian Academy of Sciences, Karelian Research Centre, Northern Water Problems Institute, Petrozavodsk, Russia

[9]University of Sussex, Department of Geography, Permafrost Laboratory, Brighton, UK

Correspondence

Sebastian Wetterich, Alfred Wegener Institute Helmholtz Centre for Polar and Marine Research, Telegrafenberg A45, D-14473 Potsdam, Germany

Email: sebastian.wetterich@awi.de

Abstract

Ground ice and sedimentary records of a pingo exposure reveal insights into Holocene permafrost, landscape and climate dynamics. Early to mid-Holocene thermokarst lake deposits contain rich floral and faunal palaeo-assemblages, which indicate lake shrinkage and decreasing summer temperatures (chironomid-based T_{July}) from 10.5 until 3.5 cal kyr BP with the warmest period between 10.5 and 8 cal kyr BP. Talik refreezing and pingo growth started about 3.5 cal kyr BP after disappearance of the lake. The isotopic composition of the pingo ice (–17.1 ± 0.6‰ $\delta^{18}O$, –144.5 ± 3.4‰ δD, slope 5.85, –7.7 ± 1.5‰ d excess) point to the initial stage of closed-system freezing captured in the record. A differing isotopic composition within the massive ice body was found (–21.3 ± 1.4‰ $\delta^{18}O$, –165 ± 11.5‰ δD, slope 8.13, 4.9 ± 3.2‰, d excess) and is likely related to the infill of dilation cracks by surface water with quasi-meteoric signature. Currently inactive syngenetic ice wedges formed in the thermokarst basin after lake drainage. The pingo preserves traces of permafrost response to climate variations in terms of ground-ice degradation (thermokarst) during the early and mid-Holocene, and aggradation (wedge-ice and pingo-ice growth) during the late Holocene.

Key words

BIOINDICATORS, CRYOLITHOLOGY, HYDROCHEMISTRY, STABLE WATER ISOTOPES, KHALERCHINSKAYA TUNDRA

1. INTRODUCTION

The interplay of permafrost aggradation and degradation shapes modern landscapes as it shaped past ones in vast areas of subarctic and arctic lowlands. Thus, traces of periglacial landforms preserved in permafrost deposits may contain records of past climate and landscape development. Besides climate control, also topography, hydrology, subsurface properties, vegetation and snow cover mediate permafrost conditions[1]. Since the lateglacial warming and especially during the early Holocene

thermal optimum extensive thaw took place in regions of continuous permafrost distribution[2]. Thermokarst, induced by active-layer deepening that triggered ground-ice melt and subsidence formed basins and valleys over hundreds of years. The climate-controlled response of ice-rich continuous permafrost to warming is addressed in current research[3]. Besides permafrost degradation during past and ongoing warming, concurrent permafrost aggradation and ground-ice formation is common and triggered by localised controls on the landscape scale[1]. A prominent landforms related to ground-ice formation are hydrostatic (closed-system) pingos, which might form in drained thermokarst-lake basins[4]. Due to the growth of the ice core the terrain surface and above-lying deposits dome up and have a characteristic elliptical to circular planar shape reaching heights of up to several tens of meters[5].

Pingos are common features in circum-arctic lowlands with continuous permafrost, which are rather well studied in the North-American Arctic in terms of formation[6], structure[7] and distribution[8]. Pingo growth and decay rates, age, and past distribution have been used for the reconstruction of past periglacial landscape conditions[9, 10, 11, 12]. Pingo inventories were furthermore employed in palaeo-environmental reconstructions in the Mackenzie Delta in Canada[13], on Seward Peninsula in Alaska[14, 15] and in Central Yakutia[16]. A modern spatial database shows more than 6000 pingos in a 3.5 x 10^6 km^2 region in the Eurasian Subarctic and Arctic, and links the pingo distribution to permafrost and landscape characteristics, to surface geology and morphology, and to hydrology and climate[17].

In the course of Russian-German fieldwork in 2012 in the Kolyma Lowland[18], different features of periglacial landscapes were studied including a pingo exposure near Pokhodsk (Figure 1, N69°2'18.096" E161°0'23.112"). The ice core of the pingo locally named 'Shirokovsky Kholm' became exposed because in summer 2003 a fire burnt overlying peaty soils (personal communication by Natalya Ivanovna Arbatskaya, Pokhodsk), which caused extensive melting of the massive ice, thaw slumping and slope erosion in its northern part (Figure 1d). This man-made impact was the onset of rapid pingo destruction, which now provides access to otherwise buried pingo ice, deposits

and internal structures. In order to characterise the pingo and to uncover its formation, sampling of the exposed ice, enclosing frozen deposits, and overlying soils was undertaken.

The pingo exposure and the surrounding modern thermokarst lake were studied and sampled to obtain representative information on both the thermokarst features and the pingos, which characterise large areas of the Kolyma Lowland. The study aims (1) to determine the timing of thermokarst lake and pingo development by applying radiocarbon dating, (2) to characterise palaeo-ecological and palaeo-climatic dynamics by analysing micropalaeontological proxy data to the lacustrine thermokarst deposits, and (3) to characterise the permafrost and ground-ice inventory by applying cryolithological, hydrochemical and stable isotope methods. Overall, the study seeks reconstructing Holocene landscape dynamics of thermokarst and pingo development in the Kolyma Lowland.

2. MATERIAL AND METHODS

2.1 Study region

The study site is situated in the Kolyma Lowland at the boundary between the Khalerchinskaya Tundra and the Kolyma Delta (Figure 1b). The Kolyma Delta extends mainly at 2-4 m above sea level (a.s.l.) at the mouth of the Kolyma River into the East Siberian Sea while the Khalerchinskaya Tundra, southwest of the delta, reaches up to 15-25 m a.s.l.[19]. Both regions are characterised by widespread thermokarst[19]. The Kolyma River divides into three major channels named Kolymskaya (Kamennaya), Pokhodskaya and Chukoch'ya, and numerous smaller channels[20]. The study region is mostly underlain by Neogene sand, silt, clay, peat, and gravel[21]. The Quaternary map of the region shows late Holocene marine-alluvial deposits in the Kolyma Delta, early Holocene marine-alluvial deposits in the Pokhodsk area, and late Holocene limnic-palustrine deposits in the Khalerchinskaya Tundra[22].

The subarctic continental climate of the Kolyma Lowland is characterised by high annual temperature amplitudes and low precipitation (T_{July} +7.5°C, $T_{January}$ –31.7°C[23]; P_{Annual} 290 mm,

Cherskiy, WMO station no. 25123). The region belongs to the continuous permafrost zone with ground temperatures of –7 to –5°C and a permafrost thickness reaching 100 to 300 m[24].

The main features of the surface morphology relate to annual freeze and thaw processes. Ice-wedge polygons at all development stages (low- and high-centre polygons, coalescent polygon ponds) as well as thermokarst lakes shape wide areas of the Kolyma floodplain and river terraces. Micro-relief features such as elevated rims of low-centre polygons and varying active-layer depths cause highly diverse soil-moisture distribution, which is reflected in the vegetation cover of polygon tundra in the study area[25]. Boreal aquatic plants such as *Menyanthes trifoliata*, *Comarum palustre* and several *Utricularia* species are common in wet areas while the occurrence of several boreal shrub and dwarf-shrub species including *Duschekia fruticosa*, *Chamaedaphne calyculata*, *Vaccinium* spp. and even scattered *Larix* stands indicate drier sites[26], and reflect the proximity to the northern tree line. According to the Circumpolar Arctic Vegetation Map[27], the study area is described as sedge, moss low-shrub wetland (W3) and low-shrub tundra (S2). *Salix* shrubs, mosses and grasses dominate the vegetation of the study site while in wind-protected areas *Betula nana* occurs. On the southern part of the pingo top, a bowl-like depression is vegetated by *Sphagnum* sp., *Rubus chamaemous, Vaccinium vitis-idaea*, *Veratrum lobelianum*, *Ledum decumbens* and *Chamerion angustifolium*. The soil cover is composed of Typic Historthel, Typic Sapristels, Typic Hemistels, Typic and Sphagnic Fibristels, and Typic Psammorthel reflecting different contents and degrees of decomposition of organic matter (OM) within the active layer. The thaw depth reached a maximum of 40 cm on the surface of the pingo (20 August 2012).

The studied pingo remnant still occupies about three quarters of its former extent (Figure 1d). The pingo remnant borders a thermokarst lake, which is paludified south-west of the pingo (Figure 1c, d). The largest extension of the pingo remnant is about 160 m and its height reaches up 17.6 m a.s.l. (Figure 1e); equivalent to about 12.8 m above lake level (a.l.l.).

2.2 Fieldwork

Ice and sediment samples were taken between August 19 and 22, 2012 by axe and hammer in the north-facing part of the pingo in different steep exposures of pingo-core ice and frozen sediment (Figures 2 and 3, Figure S 1). Three profiles named as 12P-1908-A, 12P-2008-A and 12P-2208-A were sampled in horizontal and/or vertical directions (Figure 3, Figure S 1). Additionally, a lake sediment short core named 80-1 (taken with UWITEC gravity corer) and water samples from the modern lake surrounding the pingo were taken at different depths. Still in the field, pH and electrical conductivity (EC) measurements of melted ice and water samples were performed using a WTW340i pocket meter equipped with a Tetracon 925 conductivity cell for EC (reference temperature: 25 °C) and Sentix 43-1 electrode for pH measurements.

2.3 Sediment and intrasedimental ice studies

Cryostructures of frozen soils formed by pore ice and small lenses of segregated ice (hereafter referred to as "intrasedimental ice") were described[28] and the gravimetric ice content was measured as a ratio of the weight difference between frozen and dried bulk sediment samples to the weight of dry samples and is expressed as a weight percentage (wt%). The grain-size distribution and OM properties (total nitrogen – TN, total organic carbon – TOC, and $\delta^{13}C$ of TOC) in sedimentary samples were measured; methods are described in detail by Wetterich et al.[29]. The ratio of TOC and TN is referred as C/N.

2.4 Radiocarbon dating

A total of 13 radiocarbon dates from the exposed sediment and two dates from a short core (core code 80-1) in the modern lake were obtained by accelerator mass spectrometry (AMS) at Poznan Radiocarbon Laboratory (Poland). Radiocarbon dates were obtained from unidentified moss, peat and plant detritus. Dates are reported as ages in calibrated radiocarbon years before present (cal yr

151 BP) by applying the calibration data set INTCAL13[30] (Table 1) as derived from the age-depth
152 modelling routine with the R BACON (Bayesian accumulation histories) software[31]. Median values
153 were taken for calculating the ages of events and zonation.
154
155 **2.5 Stable water isotopes and hydrochemistry of ground ice**
156 The stable-isotope hydrogen (δD), oxygen ($\delta^{18}O$) and the ion compositions of ground ice were
157 analysed; methods are described in detail by Fritz et al.[32]. Internal 1σ errors are less than 0.8‰ for
158 δD and 0.1‰ $\delta^{18}O$[33]. The deuterium excess (d excess)[34] is calculated as $d = \delta D - 8*\delta^{18}O$.
159 In order to classify the analytical data of the 35 massive ice samples (EC, pH, anions, cations, stable
160 isotopes; Table S 1) we used a cluster analysis. Ions with values below the detection level in more
161 than 50% of the ice samples were excluded from the analysis. Samples were normalised to account
162 for the different characteristics of the analytical data. We chose agglomerative hierarchical clustering
163 as the sample size is relatively small and no starting points or number of clusters have to be supplied.
164 To assess the significance of possible clusters, we used the pvclust R package[35] for hierarchical
165 clustering with p-values, which supplies probabilities for each edge in the cluster dendrogram.
166 Distances between samples were determined using Euclidean distance; the clustering method used
167 was "complete" (maximum distance). The approximately unbiased p-values (AU) provided by
168 pvclust are based on multiscale bootstrap resampling (100,000 times) and were used for a separation
169 into a reasonable number of clusters.
170
171 **2.6 Micropalaeontology**
172 Profile 12P-1908-A was studied for its micropalaeontological inventory of pollen, non-pollen
173 palynomorphs (NPPs), testaceans, diatoms and chironomids. Samples for pollen and NPP analysis
174 were prepared from 0.44 g to 4.0 g of sediment and processed following standard procedures[36]. Per
175 sample 300 pollen grains were counted and identified[37, 38]. For testacean (testate amoebae) analysis,

176 samples were suspended in purified water and wet-sieved (500-µm screen). Sphagnobiontic, soil-
177 eurybiontic and hydrobiontic ecological groups are distinguished based of habitat preferences[39, 40].
178 The diatom analysis followed standard techniques[41]. Up to 300 valves per sample were counted and
179 identified[42, 43]. Biogeographical and ecological characteristics of the diatom taxa are based on
180 Barinova *et al.*[44]. The coefficient of floristic similarity of taxa composition was calculated according
181 to Sorensen and Czekanovsky[45], and expressed in percentages. The reconstruction of pH is based on
182 the European Diatom Database[46]. The chironomid analysis followed standard techniques[47] and taxa
183 identification followed Wiederholm[48] and Brooks *et al.*[49]. Chironomid ecology and mean air
184 temperature values of the warmest month (T_{July}) optima were taken from Brooks *et al.*[49] and
185 Nazarova *et al.*[50, 51]. Effective occurrence numbers of chironomid taxa were estimated using the N2
186 index[52]. Air T_{July} were inferred using a chironomid-based temperature inference model[51].
187
188 **3. Results**
189 **3.1 Modern lake environment and subrecent diatoms**
190 The modern thermokarst lake surrounding the pingo has pH values between 6.4 and 6.8 and EC of 52
191 µS cm^{-1} in water samples taken at depth between 0 and 2.4 m. The 46-cm long lacustrine sediment
192 core is composed of grey and brown silts and sands with occasional plant detritus. The diatom record
193 of the upper 24 cm of the core differentiates into four zones, which are described and shown in detail
194 in Figure S 2. The lowermost zone A (24-22 cm depth) contains 12 taxa with *Staurosirella pinnata*,
195 *Eunotia incisa* and *E. praerupta* dominating. Acidophilic and cold-water species prevail. Zone B
196 (22-14 cm depth) with 53 taxa is much more diverse. Phytophylic species of the genus *Encyonema*
197 are notable. The increase of *S. pinnata* and *E. incisa* as well as rising diversity and the new appearance
198 of dominant species such as *Fragilaria construens*, *Achnanthidium minutissimum* and *Cocconeis*
199 *placentula*, indicate increasing temperatures, expansion of the growing season, and increase in
200 siliciclastic sediment supply in the catchment[44]. A total of 62 species mainly from benthic and

alkaliphilic groups were found in zone C (14-6 cm depth). Decreasing water level, rising temperature and ion content are detected. The uppermost zone D (6-0 cm depth) reflects the modern lake conditions, where 62 species are present, of which benthic and alkaliphilic species predominate. *S. pinnata* shows highest shares of the entire short core record.

3.2 Geochronology

The age information from sediment samples derives from 13 radiocarbon dates from plant material of the short core of the modern lake sediment and from three pingo profiles (Table 1). Two radiocarbon dates from 24-26 cm and 42-44 cm core depth of the core 80-1 reveal ages of 682 cal yr BP and 721 cal yr BP, respectively. The modelled age-height relation of profile 12P-1908-A based on five dates is shown in Figure S 3 and spans from about 10.5 to 3.5 cal kyr BP. Early Holocene radiocarbon dates of sediments enclosing the pingo ice from profiles 12P-2008-A and 12P-2208-A range between 10.3 to 8.5 cal kyr BP.

3.3 Cryostratigraphy

3.3.1 Profiles 12P-1908-A

The profiles 12P-1908-A is located at the western edge of the study site (Figure 3). The 12P-1908-A profile comprises a 6-m-thick sequence of frozen peat and ice layers, fine-grained lacustrine sediments and an ice wedge on top (Figure 2b, Figure S 1a). It accumulated between about 10.5 and 3.5 cal kyr BP (Figure 4, Figure S 3). Three units are distinguished by cryolithological properties. The lowermost unit A between 1.7 and 3.2 m a.l.l. exhibits light brown moss peat with non-parallel wavy lenticular cryostructures (1-2 cm thick), and encloses two segregated ice layers (20-30 cm thick) at 2.2 and 3 m a.l.l. with air bubbles 1-2 mm in diameter. Unit B between 3.2 and 5 m a.l.l. is built of bedded grey silt (single lamina up to 10 mm thick) and grey-brown plant detritus (single lamina up to 5 mm thick). At 4.6 m a.l.l. a light brown moss peat occurs. The cryostructures are non-

parallel wavy lenticular and irregular reticulate (ice lenses up to 1 mm thick and up to 20 mm long). The uppermost unit C between 5 and 6.5 m a.l.l. exhibits grey-brown silty fine-sands with peaty inclusions, and irregular reticulate cryostructures and occasional lenses of clear ice up to 1 cm thick with air bubbles up to 1 mm in diameter. The ice wedge of unit C is 1.8 m in visible width and 1.2 m in visible vertical extent and exhibits shoulders typical of syngenetic growth (Figure 2b). The ice wedge is not related to the modern surface (i.e. no evidence for recent rejuvenation and polygon pattern on the slope surface) and is therefore assumed to be inactive. The wedge ice contains numerous vertically elongated and rounded air bubbles of up to 1 mm in diameter. Its isotopic composition (n = 7) is on average –26.6 ± 0.7‰ for $\delta^{18}O$, –202.7 ± 6.0‰ for δD and 10.0 ± 0.7‰ for d excess (Figure 5a, Table 2). The hydrochemical composition of the wedge ice was estimated in the central part (sample 12P-1908-A-04-IW; Table S 1). The EC is rather low with 66 µS cm^{-1} and the pH is acidic (pH 5.7).

The grain-size of profile 12P-1908-A shows bimodal and polymodal distributions (Figure S 4). OM content varies in TOC from 6.3 to 37 wt% and in TN from 0.5 to 2.5 wt% (Figure 4, Figure S 5) with higher TOC and TN values and higher C/N in peaty samples (Figure 4). The $\delta^{13}C$ of TOC shows low variation with an average value of –28.4‰.

The ice content varies from 56 to 100 wt%. The EC of the intrasedimental ice is low at 40 µS cm^{-1} and the pH is slightly acidic (5.9). The isotope composition of intrasedimental ice with $\delta^{18}O$ of –17.9 ± 0.7‰, δD of –148.8 ± 4.4‰ and d excess of –5.8 ± 1.3‰ differs from those of the ice layers in unit A of the profile: –15.3 ± 0.3‰ for $\delta^{18}O$, –133.7 ± 2.6‰ for δD and –10.9 ± 0‰ for d excess (Figure 4, Table 2).

3.3.2 Profile 12P-2008-A

249 The profile 12P-2008-A between about 1 and 3 m a.l.l. represents the massive ice of the pingo core,
250 which has been sampled in different parts over a lateral distance of about 10 m (Figure 3).
251 Approximate sampling positions are given in Figure 3 and Figure S 1b.
252 Samples of enclosing sediments have additionally been taken (Figure S 1b) and radiocarbon-dated to
253 early Holocene ages between 10.3 and 9.2 cal kyr BP (Figure 4, Table 1). These deposits include
254 alternating beds of grey fine-sand and brownish plant detritus with peat inclusions and subvertical ice
255 veins (Figure 2c, Figure S 1b). The grain-size distribution is bimodal (Figure S 4) and organic matter
256 content is low with TOC values of 0.6 to 3.2 wt%, except for the uppermost sample of brown peat
257 with TOC of 33.3 wt% (Figure 4). C/N and $\delta^{13}C$ of TOC signatures as well as ice content and stable
258 water isotope composition are similar to those of unit B of profile 12P-1908-A.
259 The massive ice itself differs in colour and air bubble content and distribution. Clear pingo ice with
260 large crystals (up to 30x50 mm) and no bubbles occurs in places while most of the exposed pingo ice
261 contains air bubbles (up to 2 mm in diameter) with vertical, horizontal and subvertical orientation
262 (Figure 2d). Vertically oriented bubbles are often elongated. The stable water isotope composition of
263 the pingo ice shows $\delta^{18}O$ of –17.2 ± 0.8‰, δD of –145 ± 5.0‰ and d excess of –7.1 ± 2.0‰ (Figure
264 5b, Table 2). The EC of the pingo ice varies between 32 and 203 µS cm^{-1}, but reaches higher values
265 of up to 1068 µS cm^{-1} near the contact with sediment (Figure S 6c). Massive ice samples close to the
266 upper and lower sedimentary boundaries (Figure S 1b) exhibit higher concentration in major cations
267 (calcium, magnesium, sodium) and anions (chloride, hydrogen carbonate) except for sulphate, which
268 is low at the lower sediment contact (Figure S 6; Table S 1). The pH values range between 6.0 and
269 7.4 (Figure S 6d).
270
271 ***3.3.3 Profile 12P2208-A***
272 The profile 12P-2208-A exhibits parts of the pingo ice core and overlying sediments in the eastern
273 part of the outcrop between about 4 and 10 m a.l.l. over a lateral distance of about 30 m (Figure 3

and Figure S 1c, d). Most samples (12P-2208-A-01 to -23) were collected in vertical and horizontal lines (Figure S 1c).

The enclosing deposits of the massive ice are slightly bedded grey-brown and light brown poorly sorted sandy silts with rare wood, root and peat inclusions. The sediments have a bimodal grain-size distribution (Figure S 4). The cryostructure is mainly irregular reticulate. OM characteristics show rather low variation in TOC (2.9 to 7.2 wt%), C/N (12.3 to 16.1), and $\delta^{13}C$ (–28.2 to –27.8‰) (Figure 4, Figure S 5). Radiocarbon dates exhibit early Holocene ages between about 10.1 and 8.5 cal kyr BP and one redeposited subrecent age of 227 cal yr BP (Figure 4, Table 1).

The massive ice differentiates into two ice types. One is characterised by rather small crystal sizes (5 to 10 mm) with numerous small bubbles (<1 mm in diameter) non-regularly distributed, which cause the whitish appearance; sediment inclusions up to 1 cm thick were detected and horizontal layering was partly visible (Figure 2e and 2f). The second type has larger crystal sizes (20x30 mm up to 40x70 mm) and appears bluish and clear (Figure 2e and 2g). It includes rounded and larger bubbles (0.5 to 2 mm in diameter) in subvertical and horizontal layers and elongated bubbles (1 to 2 cm long) in subvertical direction (Figure 2g). Additionally, massive ice was sampled in three 'windows' located between 1.5 and 3 m a.l.l.. (Figure S 1d). The stable water isotope composition of the massive ice shows a wider scatter if compared to data from profiles 12P1908-A and 12P-2008-A with average values of –18.3± 2.1‰ for $\delta^{18}O$, –150.5 ± 11.4‰ for δD and –4.3 ± 6.1‰ for d excess (Figure 5c, Table 2). Stable isotope data of intrasedimental ice from above and within the massive ice (samples 12P-2208-A-04 and -14) fall within the range of the massive ice data (Figure 5c). The EC of the massive ice within this part of the exposure varies only between 45 and 116 µS cm^{-1} (Figure S 6c, Table S 1). The hydrochemical composition of the 12P-2208-A ice shows higher values for calcium and sulphate, especially in the upper part of the profile. Other major ion concentrations are comparable to those of the 12P-2008-A pingo ice (Figure S 6a, e). The pH is mainly neutral with values between pH 6.5 and pH 7.2 (Figure S 6d).

299

300 ***3.3.4 Sedimentary and organic matter characteristics of all profiles***

301 The granulometric data from all three profiles show mainly bimodal grain-size distributions with
302 peaks in the clay and the fine sand fractions (Figure S 4). Similar patterns have been observed in
303 shallow thermokarst lakes with little flow and the repeated deposition of sand particles from shore
304 slump activity[53]. The sediments within and surrounding the massive ice are assumed to be of
305 lacustrine origin. The C/N – $\delta^{13}C$ relationship reflecting OM origin[54] shows a narrow range in the
306 transition from lacustrine algae to terrestrial plants (Figure S 5). In addition, the TOC – C/N
307 relationship indicates a moderate correlation ($r^2 = 0.63$) of modestly to highly decomposed OM as
308 typical for lacustrine deposition in thermokarst environments[55]. The early Holocene radiocarbon
309 dates of deposits enclosing the massive ice (ranging from 10.3 to 8.5 cal kyr BP; Table 1) indicate
310 the depositional age of the lacustrine sediments, which have been present prior to the onset of pingo
311 formation.

312

313 **3.4 Palaeo-ecology of profile 12P-1908-A**

314 ***3.4.1 Pollen and palynomorphs***

315 Pollen and palynomorph assemblages from profile 12P-1908-A are subdivided into two pollen zones
316 (PZ-I and PZ-II) of which PZ-II is further sectioned into two sub-zones (P-IIa and P-IIb; Figure S
317 7a). In total, 33 pollen and spore taxa were identified. Most of the pollen grains and spores were well
318 preserved. Spores are generally rare in the record, but *Pediastrum* remains are present. The pollen
319 zone P-I (10.5 to 8 cal kyr BP; 1.7 to 5 m a.l.l.) is notable for high amounts of *Betula* sect. *Nanae*
320 (40-45%) and *Alnus fruticosa* (25-45%) pollen, and relatively low contents of Cyperaceae (5-10%)
321 and Poaceae (4-8%) pollen (Figure 6a). *Larix* pollen and *Encalypta* spores are present. The P-I is
322 interpreted as regional representation of southern shrub-tundra[56]. Shrub birch and alder dominated
323 the vegetation and larch occurred as isolated trees in vegetation cover. Summer climate slightly

warmer than today is assumed for P-I. Pollen zone P-IIa (8 to 5 cal kyr BP; 5 to 6.3 m a.l.l.) shows a decrease in *Alnus fruticosa* (up to 17%) (Figure S 6a), and the disappearance of *Larix*. Poaceae and Cyperaceae pollen dominate among herb taxa. *Ericales* pollen reaches 5%. *Artemisia*, *Potentilla* and *Rubus chamaemorus* pollen are present. *Pediastrum* have maximum 40%. The decrease in shrub alder and birch and disappearance of larch indicate climate cooling. The vegetation on a regional scale is interpreted as grass and shrub tundra. As in PZ-IIa the uppermost pollen zone P-IIb (5 to 3.5 cal kyr BP, above 6.3 m a.l.l.) is marked by lower counts in both *Betula* sect. *Nanae* and *Alnus fruticosa* pollen if compared to PZ-I. Cyperaceae (20-40%) and Poaceae (10%) pollen dominate (Figure S 7a). Rosaceae has higher counts than in P-IIa and *Comarum*, *Rubus chamaemorus*, *Artemisia* pollen and *Sphagnum* spores are present. Based on changes in intrazonal taxa, i.e. the decrease in *Pediastrum* and the increase in Cyperaceae, P-IIb is interpreted as local vegetation change in response to paludification and acidification of the thermokarst lake basin. *Pediastrum* remains are absent in peaty layers at 1.7 and 4.6 m a.l.l., but present in sand and silt layers of PZ-IIb indicating aquatic deposition.

3.4.2 Testaceans (testate amoebae)

In total 30 testacean taxa were identified in 10 samples of profile 12P-1908-A (Figure S 7b) including sphagnobiontic, soil-eurybiontic, and hydrobiontic species. The latter constitute the largest part of identified taxa with 24 taxa. Count numbers range between 7 and 45 specimens per sample and are therefore plotted and interpreted as presence-absence information. The testacean data of the lowermost testacean zone T-I (10.5 to 8 cal kyr BP; 1.7 to 5 m a.l.l.) indicate an aquatic habitat by prevailing presence of 11 hydrobiontic species mainly of the genera *Centropyxis* and *Difflugia* (Figure S 7b). *Sphagnum*-moss inhabiting *Trigonopyxis arcula* and *Centropyxis aculeata* indicate wet conditions. In T-II (8 to 5 cal kyr BP; 5 to 6.3 m a.l.l.) the taxa number decreases to 11, nine of which belong to hydrobiontic and two to soil-eurybiontic species. Sphagnobiontic species are

lacking. The species composition changes at sub-species level and aquatic conditions are still present. The uppermost T-III (5 to 3.5 cal kyr BP, above 6.3 m a.l.l.) reveals 16 taxa including 14 hydrobionts. The eurybiontic *Trinema lineare* and the sphagnobiontic *Centropyxis aculeata* are present. Shallow-water to semi-aquatic conditions is assumed.

3.4.3 Diatoms

In eight samples from the profile 12P-1908-A, 107 diatom taxa were found, while in assemblages of the short core of the modern lake sediments (Figure S 2) 86 taxa were present with a floristic similarity between both records of 50.8%. In zone D-I (10.5 to 8 cal kyr BP; 1.7 to 5 m a.l.l.), 41 taxa were identified. The number of species increased from 15 per sample in the lower part of the zone to 28 at the top. In the lower part of D-I, the highest percentage of planktonic and alkalibiontic species was marked, with the benthic *Cymbopleura inaequalis* associated with macrophytes as dominat species (Figure S 7c). The planktonic *Aulacoseira ambigua* indicates considerable water depth of a mature thermokarst lake around 10 cal kyr BP, which decreases afterwards. In the middle and upper parts of D-I, shares of mesohalobic, halophilic and streaming-water species increase, and alkaliphilic taxa replace alkalibiontics. The largest share of thermophilic species is observed in the upper part of D-I. Another dominant species *S. pinnata* appears and the number of subdominant *Martyana martyi*, *Amphora libyca*, *Gyrosigma acuminatum* increases. The reconstructed pH varies from 6.9 to 7.6 in D-I (Figure 6). The diatom assemblages of D-I reflect warming, increasing evaporation and ion content, and decreasing water level of a mature thermokarst lake with a littoral zone of macrophytes. Smaller species reflecting the instability of the environment replace large-sized dominant species in D-I. Diatom zone D-II (8 to 6 cal kyr BP; 5 to 5.7 m a.l.l.) exhibits a gradual increase in the species number (45 in total, ranging from 27 to 30 per sample) and increasing shares of benthic and planktonic-benthic species (Figure 6). The highest percentage of boreal species not adapted to streaming water and the lowest percentage of mesohalobic and halophilic species is observed in D-II.

374 Thermophilic species are lacking while eurythermal and cold-water species appear in the upper part
375 of the D-II. The reconstructed pH varies little from 7.9 to 8 (Figure 6). *S. pinnata* dominates the
376 lower part of D-II while *Navicula vulpina* has high counts in the upper part (Figure S 7c). Diatom
377 assemblages of D-II reflect cooling of a still-water shallow lake with reduced ion content.
378 In D-III (6 to 3.5 cal kyr BP, above 6.3 m a.l.l.) the maximum species number (51 in total, ranging
379 from 26 to 33 per sample) is notable. D-III is characterised by the highest share of planktonic-benthic
380 and acidophilic species indicating shallow water and decreasing pH (Figure 6). Eurythermal and
381 cold-water species prevail while the share of boreal species is reduced. The reconstructed pH drops
382 from 7.6 to 6.9. The major dominant of D-III is *S. pinnata*. The diatom record of D-III reflects colder
383 conditions than in D-II and D-I. The existence of a shallow lake remnant or paludified pond with low
384 ion content is assumed.
385
386 ***3.4.4 Chironomids***
387 A total of 420 head capsules, which belong to three subfamilies (Chironominae, Orthocladiinae,
388 Tanypodinae), was examined in ten samples from profile 12P-1908-A. The chironomid zone C-I
389 (10.5 to 8 cal kyr BP; 1.7 to 5 m a.l.l.) is diverse and represented by taxa indicative of cool to
390 temperate conditions (*C. anthracinus*-type, *O. consobrinus*-type, *Micropsectra insignilobus*-type), of
391 warm conditions (*Cricotopus laricomalis*-type, *Parakiefferiella bathophila*-type) and taxa associated
392 with macrophytes. Most of phytophilic taxa appear only in C-I: *Zalutschia mucronata*-type, *Z.*
393 *zalutschicola*-type, *Endochironmus impar*-type, *Polypedilum sordens*-type, and *Glyptotendipes*
394 *barbipes*-type. In the upper part of C-I (after about 9 cal kyr BP), a high number of taxa tolerant to
395 acidification and phytophilic taxa of *P. penicillatus*-type and *P. sordidellus*-type occur (Figure 6d).
396 The reconstructed mean air T_{July} reaches 10.2 to 11.4 °C. The water body was vegetated by
397 macrophytes. High abundances of acidophilic taxa indicate initiating of paludification at the
398 lakeshore. The chironomid zone C-II (8 to 5 cal kyr BP; 5 to 6.3 m a.l.l.) shows decline in taxonomic

399 diversity after 8 cal kyr BP. The abundance of the *C. anthracinus*-type is highest in the record. Many
400 phytophilic taxa disappear from the record and the taxa indicative of warm conditions are replaced
401 by the cold-stenotherm taxa (*Sergentia coracina*-type and *T. lugens*-type) indicating cooling and
402 decrease of the macrophyte belt. Summer climate cooling is reconstructed with mean T_{July} of 7.7 to
403 8.7 °C (Figure 6). Chironomid diversity in zone C-III (5 to 3.5 cal kyr BP, above 6.3 m a.l.l.) further
404 decreases with a strong shift in the taxonomic composition. In zone C-III dominant taxa are
405 phytophilic (*Cricotopus intersectus*-type), tolerant to acidification (*P. penicillatus*-type, *Zalutshia*
406 type B) and are associated with very shallow water in the littoral of the lakes (*Limnophyes* –
407 *Paralimnophyes* and *Paraphaenocladius-Parametriocnemus*). The latter two taxa can survive even
408 under semi-terrestrial conditions. The reconstructed T_{July} of C-III with 7.6 to 7.9 °C is close to
409 modern T_{July} of 7.5 °C (Figure 7). The prevalence of shallow water or semi-terrestrial taxa in C-III
410 suggests on-going disappearance of the lake.
411
412 ## 4. DISCUSSION
413 ### 4.1 The early to mid-Holocene thermokarst lake archive (10.5 to 3.5 cal kyr BP)
414 The Holocene sequence obtained in profile 12P-1908-A captures thermokarst lake deposits that
415 accumulated prior to formation of the studied pingo. The oldest date of 10,489 cal yr BP from the
416 peat underlying the lake sediment likely represents the early Holocene thermokarst onset in a
417 palustrine environment with increasing wetness and starting thaw subsidence due to ground-ice melt
418 leading to the formation of the thermokarst lake. The timing of this thermokarst initiation falls into
419 the age range from 14 to 9 cal kyr obtained from basal peat of thermokarst basins in Beringia[2]
420 reflecting lateglacial to early Holocene warming. According to the established age-height relation
421 (Figure S 3), continuous sedimentation within the lake is assumed between about 10.5 and 3.5 cal
422 kyr BP.

423 The palaeo-environmental inventory of early to mid-Holocene deposits exposed in profile 12P-1908-
424 A exhibits species-rich floral and faunal assemblages. The species distribution of each studied group
425 allows for zonation into three ecological zones (Table 3, Figure 6). The micropalaeontological
426 records reflect a thermokarst lake system with changing conditions in water level, air and water
427 temperature and water chemistry over time corresponding to Holocene variations in climate
428 conditions superimposed by local controls[32, 53] (Table 3). All palaeontological proxy data
429 differentiate the lowermost interval between about 10.5 and 8 cal kyr BP, as ecological zone I.
430 Warmer-than-today mean T_{July}, shallowing of the water body, increasing ion content and neutral pH
431 are reflected in proxy data. The lake littoral was vegetated by macrophytes and the regional
432 vegetation was southern shrub tundra. The deduced warmest conditions during the early Holocene
433 between about 10.5 and 8 cal kyr BP in the Kolyma Lowland likely correspond to earlier findings
434 along north-to-south transect at the Lena River, where lake sediments were employed to reconstruct
435 summer climate[57]. Biskaborn et al.[57] showed warmest conditions during the early Holocene in the
436 northernmost locations of the transect, in the Lena Delta. However, detailed Holocene climate
437 reconstructions along the Kolyma River are lacking, and the pattern observed along the Lena River
438 cannot be proven.
439 The ecological zone II spans from about 8 to 5 cal kyr BP according to pollen, testacean and
440 chironomid data while diatom data support a termination of zone II at about 6 cal kyr BP. Summer
441 cooling is mirrored by a vegetation change to grass-shrub tundra with decreased *Alnus* and *Betula*
442 counts, and lacking *Larix*. T_{July} reached 7.7 – 8.7 °C and cold-adapted aquatic species replaced
443 warm-adapted ones. The lake was shallow and with a decreased macrophyte belt.
444 The ecological zone III spans from about 6-5 cal kyr BP to 3.5 cal kyr BP. Sedge-shrub tundra
445 prevailed at least in the surroundings of the lake. T_{July} reached close-to-modern values: 7.6–7.9 °C.
446 Semi-aquatic conditions, low ion content and decreasing pH indicate disappearance of the lake and

starting paludification, which was the precondition for pingo formation triggered by refreezing of the talik beneath the lake.

4.2 The late Holocene pingo and wedge ice archives (3.5 cal kyr BP to present)

Until now there are only few records from pingo ice stable isotope and hydrochemical signatures[58, 59, 60]. Previous studies of pingo ice suggest vertical gradients in stable-isotope values, which depend on the original isotopic composition and availability of migrating water in the talik, the latter resulting in varying equilibrium conditions and isotopic fractionation during freezing[59]. General trends and stages are described as follows[59]: (1) rapid freezing of water in the basin sediments after drainage initiates ice formation with increasing $\delta^{18}O$ and δD and decreasing d excess; (2) talik water migration towards the freezing front under hydrostatic conditions results in ice segregation and intrusion, which is shown in large variation in $\delta^{18}O$, δD and d excess; and (3) freezing of a more and more limited volume of talik water under hydrostatic (equilibrium) conditions results in a decrease in $\delta^{18}O$ and δD and increase in d excess which follows the Rayleigh-type fractionation between water and ice. The shrinking reservoir becomes increasingly depleted in heavy isotopes as freezing continues[61].

Neither a clear gradient nor a distinct spatial pattern of stable isotope and hydrochemical data in the pingo ice are seen in the presented data (Figure S 6).

An agglomerative hierarchical cluster analysis comprising stable-isotope and hydrochemical variables of the 35 samples from the massive ice reveals two well-separated clusters and two samples that could not be assigned to any cluster (Figure S 8). Of those not-clustered samples, sample 12P-2008-A-06-PI has the highest values in EC (Figure S 6c), potassium, magnesium, sodium, chloride, sulphate and hydrogen carbonate (Figure S 6), while 12P-2008-A-12-PI has the highest pH (Figure S 6d), aluminium and fluoride values and the second highest magnesium, sodium, iron and chloride, hydrogen carbonate values (Figure S 6, Table S 1). These two ice samples are in close contact to the surrounding sediment and therefore strongly affected by sediment pore water. If we apply the results

472 of the cluster analysis to the lateral distribution of samples, we detect two areas of common chemical
473 properties (Figure 7).
474 The red cluster is well distinguishable in stable isotope signature from the green cluster, because of
475 the lower isotope ratios and the higher d excess (Figure 8): $\delta^{18}O$ (–21.3 ± 1.4‰), δD (–165.9 ±
476 11.5‰) and d excess (4.9 ± 3.2‰). Furthermore, the red cluster shows different slopes of 8.13 in the
477 $\delta^{18}O$-δD relation ($r^2 = 0.92$) and of 0.09 in the δD-d excess relation ($r^2 = 0.12$) (Figure 8) if compared
478 to the green cluster with a $\delta^{18}O$-δD slope of 5.85 ($r^2 = 0.93$) and a δD-d excess slope of -0.27 ($r^2 =$
479 0.39). The $\delta^{18}O$-δD slope of the red cluster samples is close to the GMWL and the slightly positive
480 slope in δD-d excess points to an origin different from the massive pingo ice of the green cluster.
481 Surface water from a meteoric water source that entered the massive pingo ice body might explain
482 the isotopic signature of the red cluster. Dilation cracks might have formed, filled with surface water
483 and contributed to the massive ice growth during different episodes[4]. The spatial distribution (Figure
484 7) at different heights and the relatively heavy stable isotope composition (Figure 8) of the red
485 cluster samples within profile 12P-2207-A make wedge-ice growth on the slope of the developing
486 pingo unlikely to explain the observed pattern and stable isotope composition. The red cluster
487 samples consist of whitish ice, which shows layers, sediment inclusions, small ice crystals (5 to 10
488 mm) and many small and non-regularly distributed air bubbles (<1 mm in diameter). The red cluster
489 further differs in potassium, sulphate, iron and magnesium contents from the green cluster (Figure S
490 6). The ice of the green cluster is interpreted as pingo massive ice as the data point to closed-system
491 freezing of talik water by a slope well below the GMWL in $\delta^{18}O$-δD, a negative slope in δD-d excess
492 (Figure 8) and some variation in $\delta^{18}O$ (–17.1 ± 0.6‰), δD (–144.5 ± 3.4‰) and d excess (–7.7 ±
493 1.5‰). The available pingo ice data were obtained from a lateral position and do not represent a
494 vertical profile of the central part of the ice core. Thus, not the entire freezing of the pingo ice and
495 respective variations in stable isotope composition are captured in the present record. However,
496 comparable slopes as in the green cluster were observed for mature and final stages of slow

497 equilibrium freezing of pingo ice: 5.11 in section 2 of Pestsovoye Pingo and 5.63 in section 3 of
498 Weather Pingo[59] and 5.84 in section 4 of Arsain Pingo[58]. During equilibrium freezing of water, the
499 resultant ice samples are aligned along a freezing slope that will be lower than the GMWL. Jouzel
500 and Souchez[62] observed that the slope of the freezing line depends on the initial isotopic
501 composition, with the more depleted waters producing a lower slope value. The initial δ-value of the
502 parent water is the intercept between the freezing slope and the LMWL or GMWL[62, 63], which is here
503 at about –25.5‰ $\delta^{18}O$ and –193‰ δD (Figure 8a). Further information is provided by an
504 examination of the δD-d excess relation. A negative relation between d excess and δD ($y = -0.27x - 46.58$; $r^2 = 0.39$) is found because the freezing slope has a lower value than the GMWL (Figure 8b).
505
506 Here, d excess variability is a result of the freezing conditions (freezing rate, boundary layer
507 thickness, percentage of freezing of the reservoir)[63]. As freezing progresses, the δD values of the ice
508 become progressively lower. This is accompanied by a concurrent increase in d excess values
509 (Figure 8b) and might therefore account for the initial stage of closed-system freezing[64]. The
510 deviation from the theoretical freezing slope is interpreted as expression of differing isotopic
511 fractionation during stepwise segregation of the pingo ice while refreezing of the talik. It is also
512 possible that multiple smaller ice bodies developed in the single pingo, having their own isotopic
513 boundary conditions, but taken together it provides a coherent picture of pingo development.
514 Intrasedimental ice values generally fall within the range of the massive pingo ice values (Figure 5).
515 Such similarity is reasonable because both ice types belong together genetically, as both originate
516 from ice segregation in the same talik and the same parent water.
517 Based on its stratigraphic position the ice wedge topping profile 12P-1908-A is of late Holocene age
518 and indicates permafrost aggradation during that time. Its stable-water isotope composition with
519 narrow ranges of $\delta^{18}O$ (–26.6 ± 0.6‰), of δD (–202.7 ± 5.5‰), its d excess of 10 ± 0.7‰ and its
520 position close to the GMWL (slope of 8.87; Figure 8a) confirms the wedge-ice water source from
521 precipitation. These stable-water isotope parameters further corroborate that the wedge-ice signal

522 from winter season precipitation in the region during the late Holocene averages about –26.6‰ in
523 $\delta^{18}O$, which is assumed to be mainly influenced by Pacific moisture. In contrast, the winter
524 precipitation in the Laptev Sea region is thought to be mainly fed by Atlantic moisture[65], leading to a
525 spatial pattern in late Holocene wedge-ice data with most depleted isotope values in the easternmost
526 location along a west-to-east transect. This corresponds to the continental effect in atmospheric
527 precipitation[34] as seen in decreasing $\delta^{18}O$ from Taymyr Peninsula[66] (mean $\delta^{18}O$ of –23.0‰), to the
528 Lena Delta[67, 68] (mean $\delta^{18}O$ of –24.6‰) and to Bykovsky Peninsula[65] (mean $\delta^{18}O$ of –28.5 to –
529 26.1‰). The meeting influence of moisture originating from both the Atlantic and Pacific Oceans is
530 found in the Dmitry Laptev Strait region[69] (mean $\delta^{18}O$ of –25.4 to –25.0‰).
531 The late Holocene terrestrial landscape evolution of the Kolyma Lowland is characterised by widely
532 distributed processes of permafrost aggradation, which is especially expressed in ground-ice
533 formation within drained thermokarst basins and on floodplains. Pingo growth and the formation of
534 ice-wedge polygons shaped the topography on different scales.
535
536 **4.3 The modern landscape of the Kolyma Lowland**
537 A remote-sensing based mapping of the Kolyma Lowland southwest of the delta estimates that 65%
538 of the study area are covered by Holocene thermokarst basins[70]. Similar extensive thermokarst-lake
539 basins distribution is expected in the Kolyma Delta and the Khalerchinskaya Tundra, where
540 comparable studies are lacking[71]. Grosse and Jones[17] mapped about 700 pingos in the Kolyma
541 Lowland (150.7–162.5°E) including the delta. However, the pingo 'Shirokovsky Kholm' was not part
542 of their study, since it is not expressed on topographic maps at a 200k scale. This indicates a larger
543 number of yet undocumented pingos in the Kolyma Lowland. Pingo-induced relief inversion
544 frequently led to renewal of thermokarst lakes, and secondary late Holocene thermokarst developed
545 in pre-defined basins of early Holocene age where wedge-ice melt occurred.

546 Main areas of the Kolyma Lowland such as the Khalerchinskaya Tundra and the Kolyma Delta are
547 shaped by intense thermo-erosion and thermokarst as expressed by channels, basins and shallow
548 lakes. Pingos are common features reaching 150-200 in diameter and 15-20 m in height[19] matching
549 the dimensions of the studied pingo (Figure 1e). Ice-wedge polygons occur commonly in wetlands
550 surrounding the lakes and indicate permafrost aggradation during the late Holocene.
551 The host material is mainly silt and silty sand of Holocene marine and alluvial origin in the Kolyma
552 Delta[22] and of late Holocene limnic-palustrine or aeolian origin overlying LGM alluvial and aeolian
553 sand in the Khalerchinskaya Tundra[19, 22]. Lakes of the Kolyma Delta reach huge dimensions such as
554 the largest lake of Yakutia, Lake Nerpich'e[19] covering an area of 225 km² (Figure 1b). Large
555 thermokarst lakes of the Khalerchinskaya Tundra occupy up to 38 % of the area[19] and often have
556 triangular shapes where the baseline of the triangle is more or less E-W oriented, likely preserving
557 the shoreline and lagoons of the palaeo-Kolyma Delta. The variability of thermokarst lakes in shape
558 and depth is probably connected to the host material, its ice content and the timing of delta
559 formation. This is also reflected in the Landsat-based trend analysis of lake dynamics by Nitze et
560 al.[72], where the Khalerchinskaya Tundra west of the Kolyma River mouth showed widespread lake-
561 area loss in nearly the entire region, being consistent with our reconstruction of constant
562 paludification at the lakeshore. In contrast, the Kolyma River floodplain is dominated by
563 predominantly lake expansion dynamics. While the Khalerchinskaya Tundra might represent an
564 older delta formation, comparable to the Arga Complex (2nd river terrace) of the Lena Delta[73], and
565 thermokarst there started already during lateglacial to early Holocene warming, the recent and
566 modern parts of the Kolyma Delta formed during the late Holocene and consequently thermokarst
567 lakes here are much younger. In this context, the early Holocene age of the thermokarst lake deposits
568 in the pingo exposure align it to the Khalerchinskaya Tundra. The studied complete inventory of
569 primary and secondary thermokarst and of pingo and wedge-ice growth during the different stages of
570 the Holocene is assumed representative for postglacial landscape evolution in the Kolyma Lowland.

571

572 ## 5. CONCLUSIONS

573 Early to mid-Holocene lacustrine deposits, and late Holocene wedge ice and pingo ice represent a
574 comprehensive archive of permafrost degradation and aggradation features in the Kolyma Lowland.
575 Main patterns in Holocene climate variations and permafrost response are preserved in the proxy
576 records. Thermokarst lake and palustrine deposits dated from about 10.5 to 3.5 cal kyr BP
577 differentiate into three palaeo-ecological periods. Warmest summer conditions are reconstructed for
578 the early Holocene between 10.5 and 8 cal kyr BP. Vegetation changed from southern shrub tundra
579 to grass-shrub and sedge-shrub tundra following a T_{July} cooling from 11.4 – 10.2 °C (10.5 to 8 cal kyr
580 BP) to 8.7 – 7.7 °C (8 to 5 cal kyr BP) and 7.9 – 7.6 °C (5 to 3.5 cal kyr BP). Testacean, chironomid
581 and diatom data of the lake deposits recorded decreasing water level, and diatom-based pH
582 reconstructions vary between 6.9 and 8 over time. After disappearance of the lake at about 3.5 cal
583 kyr BP, paludification of the lake's basin promoted talik refreezing and pingo growth. Stable water
584 isotope and hydrochemical signatures have recorded two types of massive ground ice. The pingo ice
585 isotopic signature points to the initial stage of closed-system freezing with a slope of 5.85. Within the
586 pingo ice, a second ice type was observed with more depleted values in $\delta^{18}O$ and δD and a slope of
587 8.13. This ice might have formed as infill of dilation cracks by surface water with quasi-meteoric
588 isotopic composition. The late Holocene wedge-ice $\delta^{18}O$ average value was about –26.6‰; moisture
589 source is assumed to derive mainly from the Pacific Ocean.
590 On the one hand, climate warming in the early Holocene has caused thermokarst lake formation. On
591 the other hand, late Holocene cooling, talik refreezing and environmental changes such as peat
592 accumulation have led to permafrost aggradation (i.e. pingo and wedge-ice development), thus
593 further intensifying a small-scale landscape mosaic of lakes, pingos and polygonal ground with
594 strong environmental gradients.
595

Acknowledgements

Members of the Arbatsky family, Liudmila Pestryakova and Mikhail Cherosov (North-eastern Federal University Yakutsk), Viktor Sitalo (St. Petersburg State Pedagogical Herzen University), and other members of the field team supported the study during fieldwork in 2012 in the Pokhodsk area. We acknowledge Caroline Höpfner (Department of Geography, Humboldt University Berlin, Germany), Dyke Scheidemann, Antje Eulenburg, Lutz Schönicke and Mikaela Weiner (all AWI Potsdam) for laboratory work. The study was part of the German–Russian joint project *Polygons in tundra wetlands: state and dynamics under climate variability in tundra regions* (Russian Foundation of Basic Research, RFBR grant no. 11-04-91332-NNIO-a and Deutsche Forschungsgemeinschaft, DFG grant no. HE 3622/16-1). The study contributes to the *Arctic Ecological Network (Arc-EcoNet)* funded by the German Federal Ministry of Education and Research (BMBF grant no. 01DJ14003 to SW). Testacean analysis was supported by RFBR (grants no. 16-04-00451-a and no. 15-29-02518 to AB). Pollen analysis was carried out at St. Petersburg State University (grant no. 18.40.68.2017 to LS). Chironomid analysis was supported by DFG (grant no. NA 760/5-1 to LN) and Russian Science Foundation (RSF grant no. 16-17-10118 to LN). TO and SW acknowledge funding from DFG (grant no. OP 217/3-1 and WE4390/7-1, respectively). The ArcticDEM was provided by the Polar Geospatial Center under NSF OPP awards 1043681, 1559691 and 1542736. We acknowledge Copernicus Sentinel Data 2017. The data presented in this paper are available at PANGAEA[74] (https://doi.org/10.1594/PANGAEA.884369). We acknowledge one anonymous reviewer and Mikhail Kanevskiy (University of Alaska Fairbanks) for critical and helpful suggestions, which improved the final version of the paper.

References

620 1 Shur YL, Jorgenson MT. 2007. Patterns of permafrost formation and degradation in relation to
621 climate and ecosystems. *Permafrost and Periglacial Processes* 18: 7-19.
622 2 Walter Anthony KM, Zimov SA, Grosse G, Jones MC, Anthony P, Chapin III FS, Finlay JC, Mack
623 MC, Davydov S, Frenzel P, Frolking S. 2014. A shift of thermokarst lakes from carbon sources to
624 sinks during the Holocene epoch. *Nature* 511: 452-456.
625 3 Koven CD, Schuur AG, Schädel C, Bohn TJ, Burke EJ, Chen G, Chen X, Ciais P, Grosse G,
626 Harden JW, Hayes DJ, Hugelius G, Jafarov EE, Krinner G, Kuhry P, Lawrence DM, MacDougall
627 AH, Marchenko SS, McGuire AD, Natali SM, Nicolsky DJ, Olefeldt D, Peng S, Romanovsky VE,
628 Schaefer KM, Strauss J, Treat CC, Turetsky M. 2015. A simplified, data-constrained approach to
629 estimate the permafrost carbon–climate feedback. *Philolophical Transactions of the Royal Society A*
630 373: 20140423.
631 4 Mackay JR. 1985. Pingo ice of the western Arctic coast, Canada. *Canadian Journal of Earth*
632 *Sciences* 22: 1452-1464.
633 5 van Everdingen RE. 1998. *Multi-language glossary of permafrost and related ground-ice terms*
634 *(revised 2005)*. National Snow and Ice Data Center/World Data Center for Glaciology: Boulder,
635 USA.
636 6 Mackay JR. 1962. Pingos of the Pleistocene Mackenzie Delta area. *Geographical Bulletin* 18: 21-
637 63.
638 7 Yoshikawa K, Leuschen C, Ikeda A, Harada K, Gogineni P, Hoekstra P, Hinzman L, Sawada Y,
639 Matsuoka N. 2006. Comparison of geophysical investigations for detection of massive ground ice
640 (pingo ice). *Journal of Geophysical Research* 111: E06S19.
641 8 Jones BM, Grosse G, Hinkel KM, Arp CD, Walker S, Beck RA, Galloway JP. 2012. Assessment
642 of pingo distribution and morphometry using an IfSAR derived DSM, western Arctic Coastal Plain,
643 northern Alaska. *Geomorphology* 138: 1-14.

644 9 Flemal RC. 1976. Pingos and pingo scars: their characteristics, distribution, and utility in
645 reconstructing former permafrost environments. *Quaternary Research* 6: 37-53.
646 10 Mackay JR. 1986. Growth of Ibyuk Pingo, western Arctic coast, Canada, and some implications
647 for environmental reconstructions. *Quaternary Research* 26: 68-80.
648 11 Walker MD, Everett KR, Walker DA, Birkland PW. 1996. Soil development as an indicator of
649 relative pingo age, Northern Alaska, USA. *Arctic and Alpine Research* 28:352-362.
650 12 Grosse G, Schirrmeister L, Siegert C, Kunitsky VV, Slagoda EA, Andreev AA, Dereviagyn AY.
651 2007. Geological and geomorphological evolution of a sedimentary periglacial landscape in
652 northeast Siberia during the late Quaternary. Geomorphology 86: 25-51.
653 13 Hyvärinen H, Ritchie JC. 1975. Pollen stratigraphy of Mackenzie pingo sediments, N.W.T.,
654 Canada. *Arctic and Alpine Research* 7: 261-272.
655 14 Wetterich S, Grosse G, Schirrmeister L, Andreev AA, Bobrov AA, Kienast F, Bigelow NH,
656 Edwards ME. 2012. Late Quaternary environmental and landscape dynamics revealed by a pingo
657 sequence on the northern Seward Peninsula, Alaska. *Quaternary Science Reviews* 39: 26-44.
658 15 Palagushkina O, Biskaborn B, Wetterich S, Schirrmeister L, Nazarova L, Grosse G. 2017. Diatom
659 records and tephra mineralogy in pingo deposits of Seward Peninsula, Alaska. *Palaeogeography,*
660 *Palaeoclimatology, Palaeoecology* 479: 1-15.
661 16 Ulrich M, Wetterich S, Rudaya N, Frolova L, Schmidt J, Siegert C, Fedorov AN, Zielhofer C.
662 2017. Rapid thermokarst evolution during the mid-Holocene in Central Yakutia, Russia. *The*
663 *Holocene* 27: 1899-1913.
664 17 Grosse G, Jones BM. 2011. Spatial distribution of pingos in northern Asia. *The Cryosphere* 5: 13-
665 33.
666 18 Schirrmeister L, Pestryakova L, Schneider A, Wetterich S. (eds.) 2016. Studies of polygons in
667 Siberia and Svalbard. *Reports on Polar and Marine Research* 697: 1-275.

668 19 Andreev AV. 2001. *Wetlands in Northeastern Russia* (Wetlands in Russia, Volume 4). WWF,
669 Wetlands International Programme, Moscow, Russia; 296 pp.
670 20 Nikanorov AM, Bryzgalo VA, Kosmenko LS, Reshetnyak OS. 2011. The Kolyma River mouth
671 area under present conditions of anthropogenic impact. *Russian Meteorology and Hydrology* 36:
672 549-558.
673 21 Auslov BN, Potshova MN, Ivanenko GV. 1998. Map of pre Quaternary deposits (R-(55)-57
674 (Nizhnekolymsk), scale 1:1,000,000. *State Geological Map of the Russian Federation*. Ministry of
675 Natural Resources of the Russian Federation, Moscow, Russia.
676 22 Ivanenko GV. 1998. Map of Quaternary formations, scale 1: 1,00,000. *State Geological Map of*
677 *the Russian Federation (New Series)*. Ministry of Natural Resources of the Russian Federation,
678 Cartographic Company VSEGEI, Moscow, Russia.
679 23 New M, Lister D, Hulme M, Makin I. 2002. A high-resolution data set of surface climate over
680 global land areas. *Climate Research* 21: 1-25.
681 24 Yershov ED, Kondratyeva KA, Zamolotchikova SA, Trush NI, Dunaeva Ye N. 1999.
682 *Geocryological map of Russia and neighboring republics, scale 1:2,500,000* . Moscow State
683 University, Russian Ministry of Geology: Moscow, Russia.
684 25 de Klerk P, Theuerkauf M, Joosten H. 2017. Vegetation, recent pollen deposition, and distribution
685 of some non-pollen palynomorphs in a degrading ice-wedge polygon mire complex near Pokhodsk
686 (NE Siberia), including size-frequency analyses of pollen attributable to *Betula*.
687 *Review of Palaeobotany and Palynology* 238: 122-143.
688 26 Kienast F. 2016. Studies of modern vegetation and sampling of permafrost deposits for
689 palaeobotanical studies at the lower Kolyma. *Reports on Polar and Marine Research* 697: 87-160.
690 27 CAVM Team (2003) *Circumpolar Arctic vegetation map (1:7,500,000 scale). Conservation of*
691 *Arctic Flora and Fauna (CAFF) Map No. 1*. US Fish and Wildlife Service: Anchorage, Alaska,
692 USA. Last access: 18 January 2017, http://www.geobotany.uaf.edu/cavm/.

693 28 French H, Shur Y. 2010. The principles of cryostratigraphy. *Earth-Science Reviews* 101: 190-
694 206.
695 29 Wetterich S, Tumskoy V, Rudaya N, Kuznetsov V, Maksimov F, Opel T, Meyer H, Andreev AA,
696 Schirrmeister L. 2016. Ice Complex permafrost of MIS5 age in the Dmitry Laptev Strait coastal
697 region (East Siberian Arctic). *Quaternary Science Reviews* 147: 298-311.
698 30 Reimer PJ, Bard E, Bayliss A, Beck JW, Blackwell PG, Bronk Ramsey C, Buck CE, Cheng H,
699 Edwards RL, Friedrich M, Grootes PM, Guilderson PT, Haflidason H, Hajdas I, Hattz C, Heaton TJ,
700 Hoffmann DL, Hogg AG, Hughen KA, Kaiser KF, Kromer B, Manning SW, Niu M, Reimer RW,
701 Richards DA, Scott EM, Southon JR, Staff RA, Turney CSM, van der Plicht J. 2013. IntCal13 and
702 Marine13 radiocarbon age calibration curves 0-50,000 years cal BP. *Radiocarbon* 55(4): 1869-1887.
703 31 Blaauw M, Christen JA. 2011. Flexible paleoclimate age-depth models using an autoregressive
704 gamma process. *Bayesian Analysis* 6: 457-474.
705 32 Fritz M, Wolter J, Rudaya N, Palagushkina O, Nazarova L, Obu J, Rethemeyer J, Lantuit H,
706 Wetterich S. 2016. Holocene ice-wedge polygon development in the northern Yukon, Canada.
707 *Quaternary Science Reviews* 147: 279-297.
708 33 Meyer H, Schönicke L, Wand U, Hubberten H-W, Friedrichsen H. 2000. Isotope studies of
709 hydrogen and oxygen in ground ice - experiences with the equilibration technique. *Isotopes in*
710 *Environmental and Health Studies* 36, 133-149.
711 34 Dansgaard W. 1964. Stable isotopes in precipitation. *Tellus* 16: 436-468.
712 35 Suzuki R, Shimodaira H. 2015. *pvclust: hierarchical clustering with p-values via multiscale*
713 *bootstrap resampling*. Last access: 25 October 2017, http://www.sigmath.es.osaka-u.ac.jp/shimo-
714 lab/prog/pvclust/
715 36 Berglund BE, Ralska-Jasiewiczowa M. 1986. Pollen analysis and pollen diagram. In *Handbook of*
716 *Holocene Palaeoecology and Palaeohydrology*, Berglund BE (ed). Wiley Interscience: New York,
717 USA; 455-484.

718 37 Moore PD, Webb JA, Collinson ME. 1991. *Pollen analysis*. Blackwell Scientific: Oxford, UK.
719 38 Savelieva LA, Raschke EA, Titova DV. 2013. *Photographic atlas of plants and pollen of the*
720 *Lena River Delta*. St. Petersburg State University: St. Petersburg, Russia (in Russian).
721 39 Chardez D. 1965. Ecologie générale des Thécamoebiens. *Bulletin de l'Institut Agronomique et*
722 *des Stations de Recherche de Gembloux* 33: 307-341 (in French).
723 40 Bobrov AA, Wetterich S, Beermann F, Schneider A, Kokhanova L, Schirrmeister L, Pestryakova
724 L, Herzschuh U. 2013. Testate amoebae and environmental features of polygon tundra in the
725 Indigirka lowland (East Siberia). *Polar Biology* 36: 857-870.
726 41 Battarbee RW, Jones VJ, Flower RJ, Cameron NG, Bennion H, Carvalho L, Juggins S.
727 2001. Diatoms. In *Tracking Environmental Change Using Lake Sediments*, Smol JP, Birks HJB,
728 Last WM (eds). Kluwer Academic Publishers, Dordrecht, The Netherlands; 155-202.
729 42 Krammer K, Lange-Bertalot H. 1986-1991. Bacillariophyceae, vol. 2 (1–4). In *Süsswasserflora*
730 *von Mitteleuropa*, Ettle H, Gerloff J, Heyning H, Mollenhauer D (eds). Gustav Fischer Verlag:
731 Stuttgart, Jena, Germany (in German).
732 43 Guiry MD, Guiry GM. 2017. *AlgaeBase*. National University of Ireland: Galway, Ireland. Last
733 access: 18 January 2017, http://www.algaebase.org.
734 44 Barinova SS, Medvedeva LA, Anisimova OV. 2006. *Biodiversity of Algae-Indicators of the*
735 *Environment)*. Pilies Studio: Tel Aviv, Israel (in Russian).
736 45 Magurran E. 1992. *Ecological diversity and its measurement*. Princeton University Press:
737 Princeton, USA.
738 46 European Diatom Database. 2001. *European Diatom Database*. Newcastle University: Newcastle
739 upon Tyne, UK. Last excess: 18 January 2017, http://craticula.ncl.ac.uk/Eddi/jsp/.
740 47 Brooks SJ, Birks HJB. 2000. Chironomid-inferred late-glacial and early-Holocene mean July air
741 temperatures for Kråkenes Lake, western Norway. *Journal of Paleolimnology* 23: 77-89.

742 48 Wiederholm T. 1983. Chironomidae of the holarctic region. Keys and diagnoses. Part 1. Larvae.
743 *Entomologica Scandinavica Supplements* 19:1-457.
744 49 Brooks SJ, Langdon PG, Heiri O. 2007. *Using and identifying chironomid larvae in*
745 *palaeoecology*. QRA Technical Guide № 10. Quaternary Research Association: London, UK.
746 50 Nazarova L, Herzschuh U, Wetterich S, Kumke T, Pestjakova L. 2011. Chironomid-based
747 inference models for estimating mean July air temperature and water depth from lakes in Yakutia,
748 northeastern Russia. *Journal of Palaeolimnology* 45: 57-71.
749 51 Nazarova L, Self A, Brooks SJ, van Hardenbroek M, Herzschuh U, Diekmann B, 2015. Northern
750 Russian chironomid-based modern summer temperature data set and inference models. *Global and*
751 *Planetary Change* 134: 10-25.
752 52 Hill MO. 1973. Diversity and evenness: a unifying notation and its consequences. *Ecology* 54:
753 427-432.
754 53 Biskaborn BK, Herzschuh U, Bolshiyanov DY, Schwamborn G, Diekmann B. 2013. Thermokarst
755 processes and depositional events in a tundra lake, Northeastern Siberia. *Permafrost and Periglacial*
756 *Processes* 24: 160-174.
757 54 Meyers PA. 1997. Organic geochemical proxies of paleoceanographic, paleolimnologic, and
758 paleoclimatic processes. *Organic Geochemistry* 27: 213-250.
759 55 Lenz J, Wetterich S, Jones BM, Meyer H, Bobrov A, Grosse G. 2016. Evidence of multiple
760 thermokarst lake generations from an 11 800-year-old permafrost core on the northern Seward
761 Peninsula, Alaska. *Boreas* 45: 584-603.
762 56 Klemm J, Herzschuh U, Pisaric M, Telford R, Heim B, Pestryakova LA. 2013. A pollen-climate
763 transfer function from the tundra and taiga vegetation in Arctic Siberia and its applicability to a
764 Holocene record. *Palaeogeography, Palaeoclimatology, Palaeoecology* 386: 702-713.
765 57 Biskarborn BK, Subetto DA, Savelieva LA, Vakhrameeva PS, Hansche A, Herzschuh U, Klemm
766 J, Heinecke L, Pestryakova LA, Meyer H, Kuhn G. 2016. Late Quaternary vegetation and lake

767 system dynamics in north-eastern Siberia: Implications for seasonal climate variability. *Quaternary*
768 *Science Reviews* 147: 406-421.58 Ishikawa M, Yamkhin J. 2016. Formation chronology of Arsain
769 pingo, Darhad Basin, Northern Mongolia. *Permafrost and Periglacial Processes* 27: 297-306.
770 59 Vasil'chuk YuK, Lawson DE, Yoshikawa K, Budantseva NA, Chizhova JN, Podborny YeYe,
771 Vasil'chuk AC. 2016. Stable isotopes in the closed-system Weather Pingo, Alaska and Pestsovoye
772 Pingo, northwestern Siberia. *Cold Regions Science and Technology* 128: 13-21.
773 60 Yoshikawa K, Natsagdorj S, Sharkhuu A. 2013. Groundwater hydrology and stable isotope
774 analysis of an open-system pingo in northwestern Mongolia. *Permafrost and Periglacial Processes*
775 24: 175-183.
776 61 Lacelle D. 2011. On the $\delta^{18}O$, δD and D-excess relations in meteoric precipitation and during
777 equilibrium freezing: Theoretical approach and field examples. *Permafrost and Periglacial*
778 *Processes* 22: 13-25.
779 62 Jouzel J, Souchez R. 1982. Melting and refreezing at the glacier sole and the isotopic composition
780 of the ice. *Journal of Glaciology* 28: 35-42.
781 63 Souchez RA, Jouzel J, Lorrain R, Sleewaegen S, Stievenard M, Verbeke V. 2000. A kinetic
782 isotope effect during ice formation by water freezing. *Geophysical Research Letters* 27: 1923-1926.
783 64 Fritz M, Wetterich S, Meyer H, Schirrmeister L, Lantuit H, Pollard WH. 2011. Origin and
784 characteristics of massive ground ice on Herschel Island (Western Canadian Arctic) as revealed by
785 stable water isotope and hydrochemical signatures. *Permafrost and Periglacial Processes* 22: 26-38.
786 65 Meyer H, Dereviagin AYu, Siegert C, Hubberten H-W. 2002. Paleoclimate studies on Bykovsky
787 Peninsula, North Siberia - hydrogen and oxygen isotopes in ground ice. Polarforschung 70: 37-51.
788 66 Chizhov AB, Dereviagin AYu, Simonov EF, Hubberten H-W, Siegert C. 1997. Isotope
789 composition of ground ice in the area of Labaz Lake (Taimyr). *Kriosfera Zemli* 1: 79–84 (in
790 Russian).

791 67 Wetterich S, Kuzmina S, Andreev AA, Kienast F, Meyer H, Schirrmeister L, Kuznetsova T,
792 Sierralta M. 2008. Palaeoenvironmental dynamics inferred from late Quaternary permafrost deposits
793 on Kurungnakh Island (Lena Delta, Northeast Siberia, Russia). *Quaternary Science Reviews* 27:
794 1523-1540.
795 68 Meyer H, Opel T, Laepple T, Dereviagin AYu, Hoffmann K, Werner M. 2015. Long-term winter
796 warming trend in the Siberian Arctic during the mid- to late Holocene. Nature Geoscience 8: 122-
797 125.
798 69 Opel T, Wetterich S, Meyer H, Dereviagin A Yu, Fuchs MC, Schirrmeister L. 2017. Ground-ice
799 stable isotopes at the Oyogos Yar Coast (Dmitry Laptev Strait) – indications for Late Quaternary
800 paleoclimate in the Northeast Siberian Arctic. Climate of the Past 13: 587-611.
801 70 Veremeeva A, Gubin S. 2009. Modern tundra landscapes of the Kolyma Lowland and their
802 evolution in the Holocene. *Permafrost and Periglacial Processes* 20: 399-406.
803 71 Veremeeva AA and Glushkova NV. 2016. Formation of relief in the regions of Ice Complex
804 deposits distribution: remote sensing and GIS studies in the Kolyma Lowland tundra. *Kriosfera*
805 *Zemli* 20: 14-24.
806 72 Nitze I, Grosse G, Jones BM, Arp C, Ulrich M, Fedorov A, Veremeeva A. 2017. Landsat-Based
807 Trend Analysis of Lake Dynamics across Northern Permafrost Regions. *Remote Sensing* 9: 640.
808 73 Schwamborn G, Andreev AA, Rachold V, Hubberten H-W, Grigoriev MN, Tumskoy V, Pavlova
809 EYu, Dorozhkina MV. 2002. Late Quaternary sedimentation history of the Lena Delta. *Quaternary*
810 *International* 89: 119-134.
811 74 Wetterich S, Meyer H, Nazarova LB, Palagushkina OV, Savelieva LA, Schirrmeister L, Syrykh,
812 LS. 2017. Sediment, ground ice and micropaleontological data from the pingo exposure 'Shirokovsky
813 Kholm' (Kolyma Lowland, NE Siberia) sampled in 2012. *PANGAEA*,
814 https://doi.org/10.1594/PANGAEA.884369
815

Tables

TABLE 1 AMS ^{14}C dating results. All samples are calibrated using Calib Rev 7.0.2[30], calibration data set intcal13.14c as derived from the age-depth modelling routine with the R BACON.

Sample ID	Lab ID	Height	Depth	Material	^{14}C age	^{14}C age 2σ range	^{14}Cage median
		[m a.l.l.]	[cm]		[yr BP]	[cal yr BP]	[cal yr BP]
Short core 80-1							
-13	Poz-55452		24-26	bulk OM	795 ± 30	651 – 727	**682**
-22	Poz-55453		42-44	bulk OM	850 ± 30	681 – 772	**721**
Profile 12P-1908-A							
-09	Poz-50918	6.5		moss peat	3,855 ± 35	4,000 – 4,485	**4,239**
-12	Poz-50919	5.2		bulk OM, fine plant detritus	6,850 ± 50	6,741 – 7,751	**7,616**
-14	Poz-50920	4		bulk OM, fine plant detritus	8,290 ± 50	8,650 – 9,345	**9,112**
-17	Poz-50921	2.5		moss peat	8,610 ± 50	9,586 – 10,266	**9,942**
-19	Poz-50923	1.7		moss peat	9,210 ± 50	10,276 – 11,061	**10,489**
Profile 12P-2008-A							
-01	Poz-50915	3.7		moss peat	9,190 ± 50	10,183 – 10,526	**10,337**
-04	Poz-50916	2.8		bulk OM, fine plant detritus	8,350 ± 50	9,228 – 9,474	**9,364**
-17	Poz-50917	2		bulk OM, fine plant detritus	8,230 ± 50	9,061 – 9,319	**9,204**
Profile 12P-2208-A							
-04	Poz-50911	7.1		moss fragments	8,930 ± 50	9,767 – 10,270	**10,055**
-06	Poz-50912	6.2		moss fragments	7,650 ± 50	7,836 – 8,782	**8,497**
-14	Poz-50914	4.7		moss fragments	225 ± 30	-1 – 458	**227**

TABLE 2 Stable isotope ($\delta^{18}O$, δD, and d excess) minimum, mean, maximum values, standard deviations (std), and slopes, intercept and correlation coefficient (r^2) from Figure 6 per profile.

Profile ID	Ice type	n	$\delta^{18}O$ min	$\delta^{18}O$ mean	$\delta^{18}O$ max	$\delta^{18}O$ std	δD min	δD mean	δD max	δD std	d min	d mean	d max	d std	Slope	Inter-cept	r^2
			[‰]	[‰]	[‰]	[‰]	[‰]	[‰]	[‰]	[‰]	[‰]	[‰]	[‰]	[‰]			
12-P-1908-A	Ice wedge	7	–27.59	–26.59	–25.62	0.62	–211.5	–202.7	–193.7	6.0	9.2	10.0	11.3	0.70	8.87	33.1	1
12-P-1908-A	Intrasedi-mental	11	–19.04	-17.41	-15.10	1.19	-156.7	-146.0	-131.8	7.3	-10.9	-6.8	-3.9	2.36	8,10	39.89	0.99
12-P-2008-A	Intrasedi-mental	2	–18.46	–18.17	–17.88	0.41	–154.2	–151.4	–148.6	4.0	–6.5	–5.8	–5.1	1.02	9.64	23.69	1
12-P-2008-A	Massive ice	13	–19.06	–17.24	–16.43	0.83	–156.2	–145.0	–137.9	5.0	–8.9	–7.1	–1.8	2.0	5.86	–44.04	0.96
12-P-2208-A	Intrasedi-mental	2	–21.00	-19.26	–17.52	2.46	–163.3	–156.2	–149.1	10.1	–8.9	–2.1	4.7	9.61	4.09	–77.36	1
12-P-2208-A	Massive ice	22	–23.19	–18.27	–16.69	2.07	–182.4	–150.5	–142.1	11.4	–9.3	–4.3	9.2	6.10	5.34	53.01	0.95

TABLE 3 Compiled interpretation of early to mid-Holocene palaeontological proxy data from profile 12P-1908-A.

Period	**Early Holocene**	**Early to mid-Holocene**	**Mid-Holocene**
Age	**11-8 cal kyr BP**	**8-6(5) cal yrs BP**	**6(5)-3.5 cal kyr BP**
Pollen	→ southern shrub tundra → dominating *Betula* and *Alnus* → *Larix* present → slightly warmer than today	→ grass-shrub tundra → decreased *Betula* and *Alnus* → *Larix* absent → climate cooling	→ sedge-shrub tundra → decreased *Betula* and *Alnus* → *Larix* absent → close-to-modern climate
Testacean	→ diverse hydrobionts → aquatic conditions	→ less diverse hydrobionts → aquatic conditions	→ diverse hydrobionts → semi-aquatic conditions
Diatoms	→ highest share of planktonic species → highest share of alkalibiontic and thermophilic species → decreasing water level → increasing ion content → pH 6.9 – 7.6 → warming	→ no planktonic species → increasing benthic and planktonic-benthic species → highest share of boreal species → shallow water → decreasing ion content → pH 7.9 – 8 → cooling	→ no planktonic species → highest share of benthic-planktonic species → highest share of acidophilic species → shallow water → decreased ion content → pH 6.9 – 7.6 → cooling
Chironomids	→ high diversity → dominating phytophilic taxa → lake with well-established macrophyte littoral → present warm-stenotherm taxa → T_{July} 10.2 – 11.4 °C	→ decreasing diversity → decreasing phytophilic taxa → lake with decreasing macrophyte littoral → cold-stenotherm replace warm-stenotherm taxa → mean T_{July} 7.7 – 8.7 °C	→ decreasing diversity → dominant taxa tolerant to acidification → shallow water to semi-aquatic with present macrophytes → present cold-stenotherm taxa → mean T_{July} 7.6 – 7.9 °C

837 ***Figure***

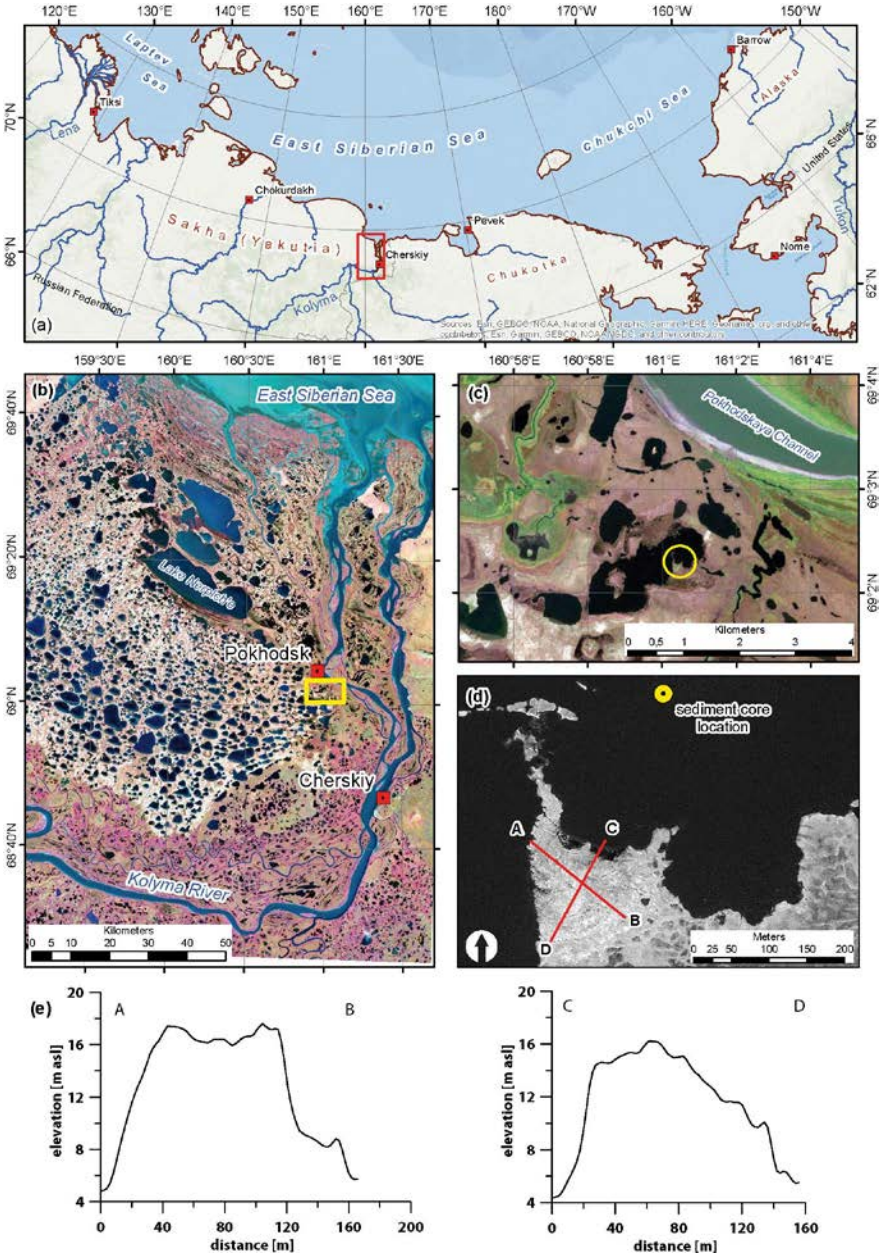

838

839 **FIGURE 1** Location of the study area (a) in the eastern Siberian Arctic, (b) on a map of the

840 Khalerchinskaya Tundra in the Kolyma Lowland (background false colour infrared image of

841 Sentinel-2, August 31, 2017), (c) in a close up view of the pingo-hosting thermokarst lake basin (true

842 colour representation) and (d) on a WorldView-1 satellite image (June 28, 2009) showing erosional

843 pingo margins along lake shore and elevation profile locations given in (e) based on ArcticDEM

844 digital elevation model data at 2 m resolution, created from a WorldView-2 stereo pair acquired on

845 April 12, 2013.

FIGURE 2 Photographs of the pingo 'Shirokovsky Kholm' showing (a) the modern lake surrounding the pingo, (b) a syngenetic ice wedge on top of profile 12P-1908-A, (c) a bedded sedimentary interlayer of profile 12P-2008-A (sample no. -03, to -05 in Figure S 1b) with verticals ice veins and peaty inclusions, (d) bubble-rich clear ice of profile 12P-2008-A (sample no. -19 in Figure S 1b), (e) the upper part of profile 12P-2208-A with close-ups of the pingo ice shown in (f) whitish ice with small ice crystals (up to 5 x 10 mm) and small bubbles (< 1mm in diameter) non-regularly distributed (sample no. -20, to -23 in Figure S 1c) and (g) clear ice with larger ice crystals (up to 20 x 30 mm) and larger bubbles (1 mm in diameter) in subvertical and horizontal layers (sample no. -19 in Figure S 1c).

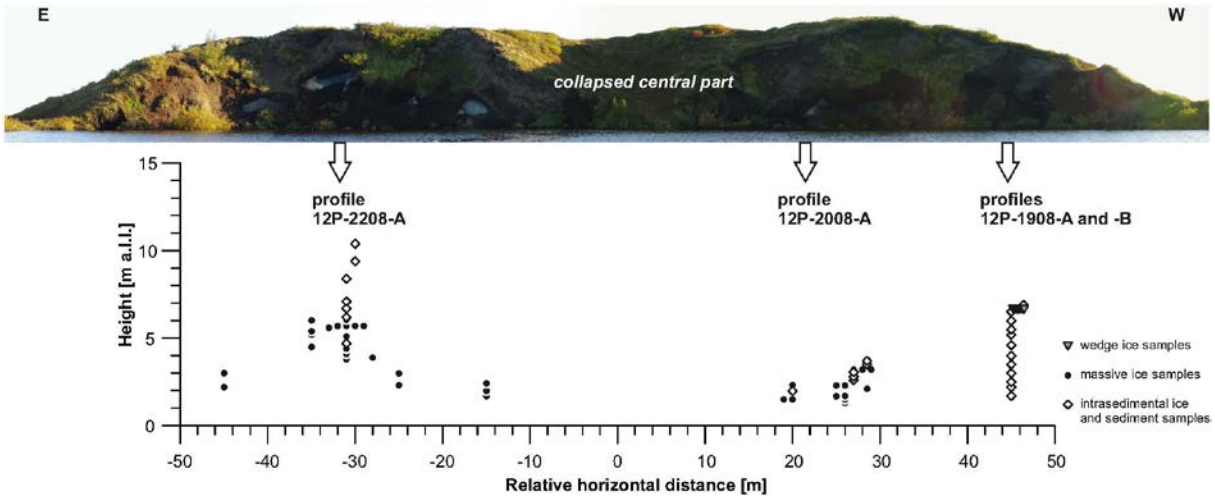

858

859 **FIGURE 3** Overview of the sampled outcrop at the pingo exposure 'Shirokovsky Kholm'. Note that

860 the photograph is not to scale. Details of the sampled profiles are given in Figure S 1.

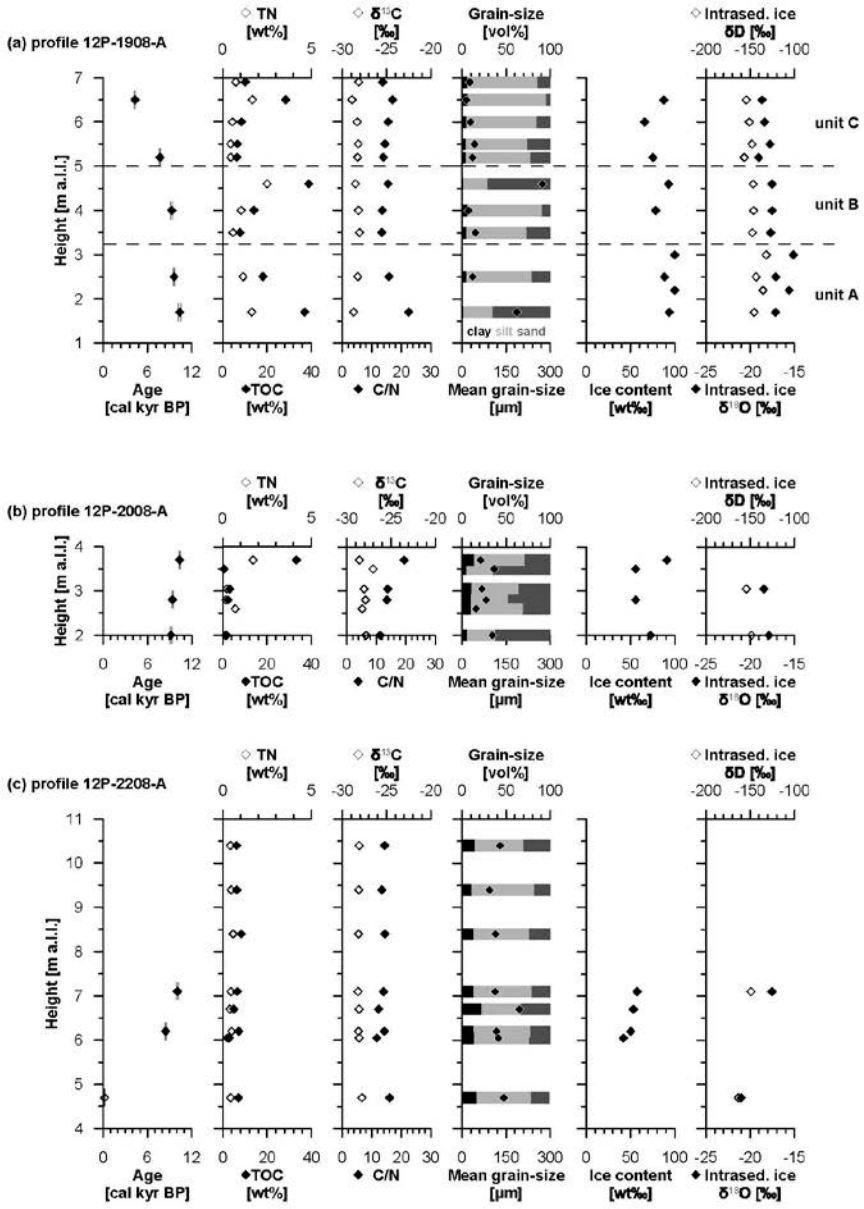

861

862 **FIGURE 4** Properties of sediments and intrasedimental ice from profiles (a) 12P-1908-A, (b) 12P-

863 2008-A and (c) 12P-2208-A. White diamond symbols refer to the respective upper x-axis.

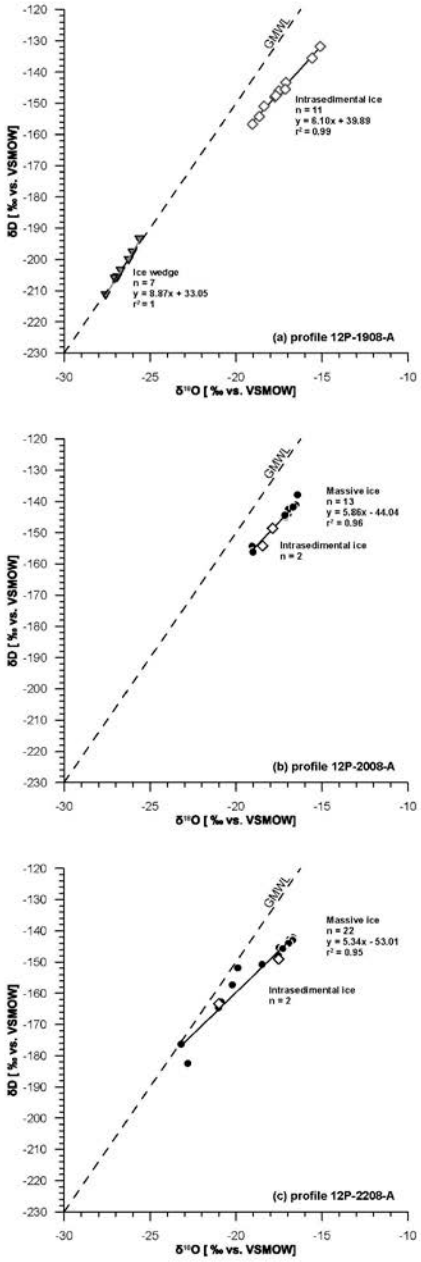

FIGURE 5 $\delta^{18}O$ and δD data of ice samples from profiles (a) 12P-1908-A, (b) 12P-2008-A and (c) 12P-2208-A. Wedge-ice data are gives as grey triangles, intrasedimental ice data are given as white diamonds and massive ice data are given as black dots. The Global Meteoric Water Line (GMWL) is given as dotted line.

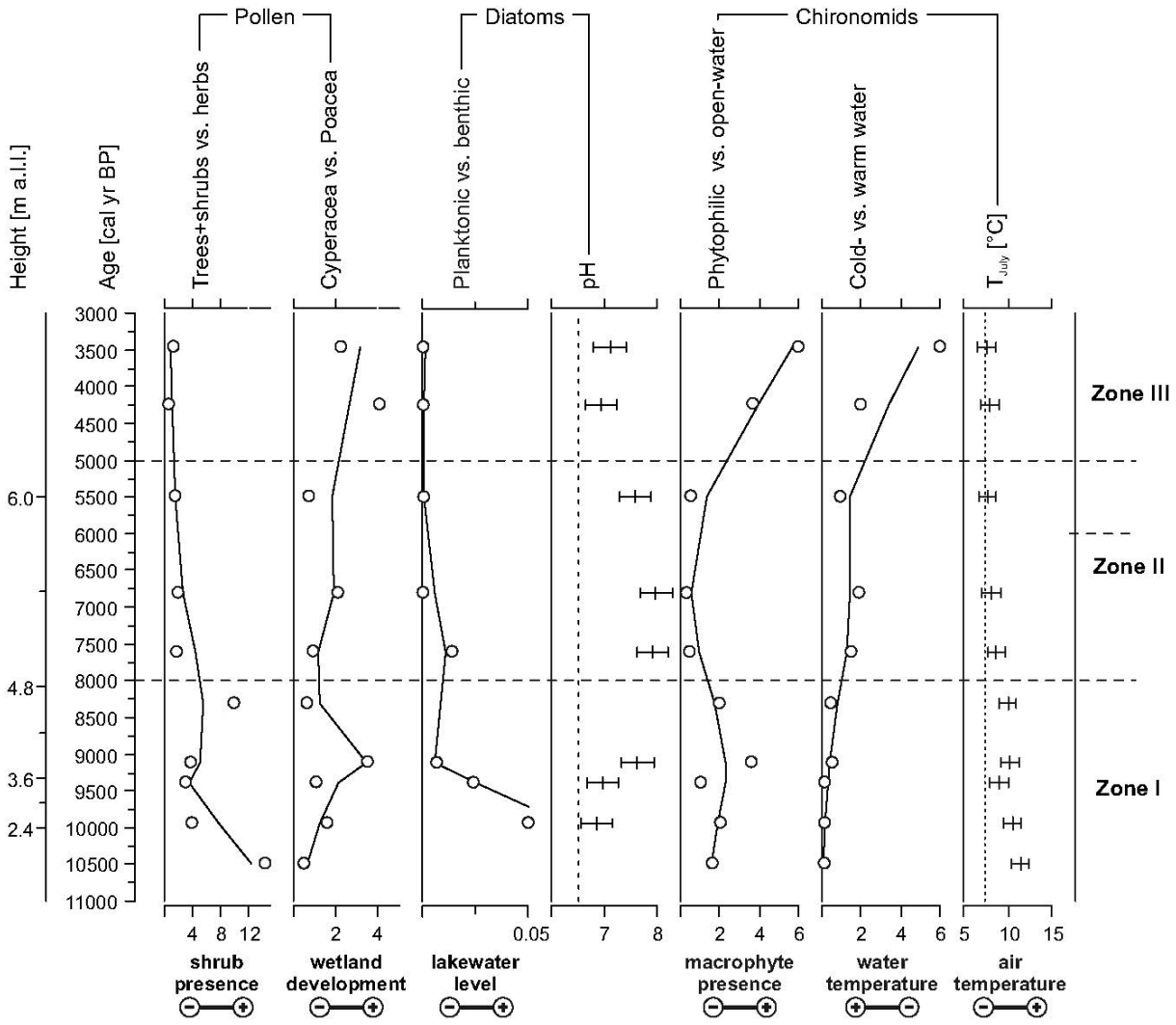

FIGURE 6 Summary of palaeo-ecological data including pollen-based ratios of Cyperaceae vs. Poaceae and trees and shrubs vs. herbs, diatom-based ratio of planktonic vs. benthic species and pH reconstruction, and chironomid-based cold-stenoterm vs. warm-stenoterm taxa, phytophilic vs. free-water taxa and T_{July} reconstruction. Black lines indicate LOESS 0.5 smooth of the data.

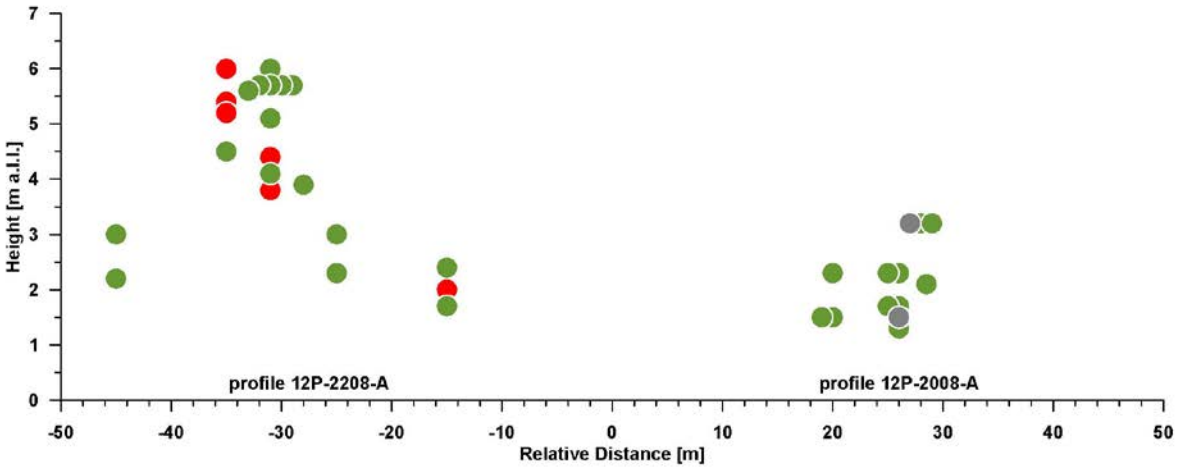

874

875 **FIGURE 7** Spatial distributions of massive-ice properties (EC, pH, anions, cations, stable-isotope
876 signature; Table S 1) according to agglomerative hierarchical clustering. Two clusters are well
877 separated (green and red; Figure S 8a, b) and two samples could not be assigned to any cluster
878 (grey).

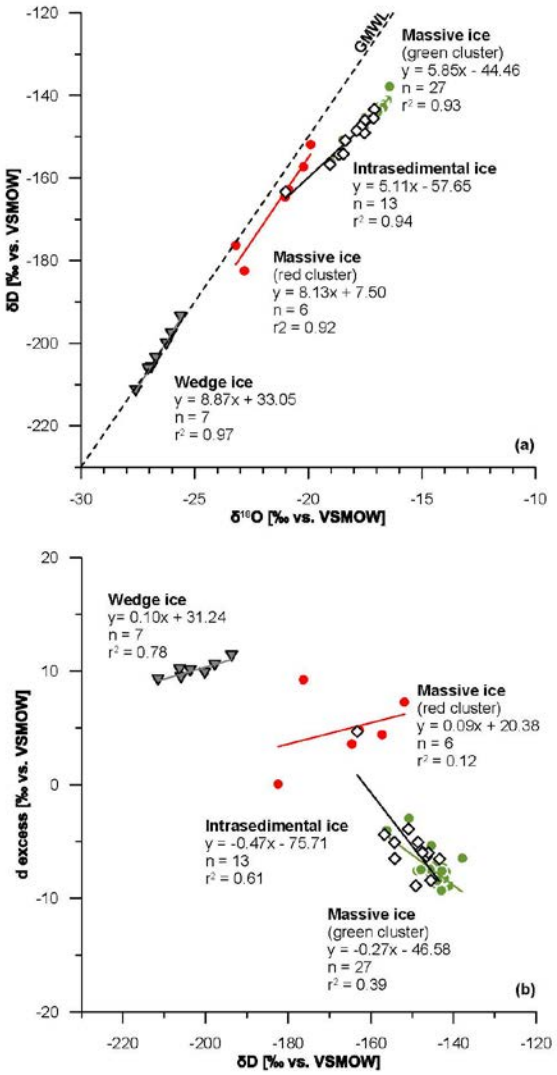

879

880 **FIGURE 8** $\delta^{18}O$, δD and d excess data of ice samples combined from all profiles as wedge ice (grey

881 triangles), intrasedimental ice (white diamonds) and massive ice (red and green dots) in a (a) $\delta^{18}O$ –

882 δD bi- plot and (b) δD – d excess bi-plot.

TABLE S 1 Hydrochemical and stable-water isotope data of massive ice (MI) and wedge ice (IW)

Sample ID	EC	pH	Al	Ca	Fe	K	Mg	Mn	Na	Sr	Zn	F	Cl	SO_4	NO_3	HCO_3	$\delta^{18}O$	δD	d excess
	µS cm^{-1}		mg l^{-1}	mg l^{-1}	mg l^{-1}	mg l^{-1}	mg l^{-1}	mg l^{-1}	mg l^{-1}	mg l^{-1}	mg l^{-1}	mg l^{-1}	mg l^{-1}	mg l^{-1}	mg l^{-1}	mg l^{-1}	‰	‰	‰
12P-1908-A-																			
-01-IW	--	--	--	--	--	--	--	--	--	--	--	--	--	--	--	--	-26.25	-200.2	9.8
-02-IW	--	--	--	--	--	--	--	--	--	--	--	--	--	--	--	--	-25.62	-193.7	11.3
-03-IW	--	--	--	--	--	--	--	--	--	--	--	--	--	--	--	--	-26.03	-197.8	10.5
-04-IW	66	5.7	0.44	5.54	0.76	1.53	1.00	0.21	1.27	0.03	0.04	0.06	4.04	16.02	0.33	1.98	-26.91	-205.9	9.4
-05-IW	--	--	--	--	--	--	--	--	--	--	--	--	--	--	--	--	-27.05	-206.3	10.1
-06-IW	--	--	--	--	--	--	--	--	--	--	--	--	--	--	--	--	-27.59	-211.5	9.2
-07-IW	--	--	--	--	--	--	--	--	--	--	--	--	--	--	--	--	-26.71	-203.7	10.0
12P-2008-A-																			
-06-MI	1068	7.3	0.05	26.80	0.82	3.26	29.00	0.30	120.0	0.32	<0.02	0.09	255.7	29.80	<0.15	71.69	-19.06	-154.3	-1.8
-07-MI	32	7.3	0.09	1.23	0.10	0.24	0.18	0.05	0.78	<0.02	<0.02	0.06	3.06	0.43	0.17	5.64	-16.43	-137.9	-6.5
-08-MI	32	7.3	0.08	1.70	0.06	<0.2	<0.1	0.05	0.31	<0.02	<0.02	0.08	2.64	0.25	<0.15	3.97	-16.53	-141.2	-8.9
-09-MI	32	7.2	0.30	1.73	0.47	0.26	0.43	0.07	1.85	<0.02	<0.02	0.11	6.87	0.39	<0.15	5.19	-16.95	-144.1	-8.5
-10-MI	30	7.2	0.09	0.75	0.09	<0.2	0.21	0.04	1.21	<0.02	<0.02	0.11	4.59	0.46	0.31	3.51	-17.02	-144.6	-8.5
-11-MI	101	6.0	0.12	2.04	0.12	0.39	2.20	0.05	8.44	0.02	<0.02	0.11	20.82	0.24	<0.15	6.71	-17.02	-144.4	-8.2
-12-MI	174	7.5	0.60	3.80	0.48	1.40	2.44	0.04	11.00	0.03	0.07	0.18	15.17	0.17	<0.15	35.24	-17.17	-145.1	-7.8
-13-MI	41	7.1	0.14	1.05	0.11	<0.2	0.19	0.04	1.98	<0.02	<0.02	0.09	7.07	< 0.10	<0.15	4.88	-16.98	-144.1	-8.3
-14-MI	35	7.4	0.06	1.02	0.04	<0.2	0.22	0.04	2.08	<0.02	<0.02	0.09	6.56	0.15	<0.15	3.20	-17.14	-145.0	-7.9
-15-MI	55	7.1	0.06	0.73	0.04	<0.2	0.21	0.04	4.79	<0.02	<0.02	0.09	11.47	< 0.10	<0.15	3.81	-16.95	-142.5	-7.3
-16-MI	74	7.0	0.09	1.43	0.09	0.25	0.73	0.04	5.74	<0.02	<0.02	0.10	15.50	0.16	<0.15	6.10	-16.69	-141.8	-7.7
-18-MI	75	7.4	0.11	2.14	0.06	0.59	1.28	0.04	7.74	<0.02	<0.02	0.11	16.57	0.14	<0.15	9.76	-17.16	-144.4	-7.1
-19-MI	203	7.4	0.08	4.55	0.08	0.67	3.97	0.06	17.20	0.09	<0.02	0.11	41.11	0.45	0.15	17.24	-19.02	-156.2	-4.0
12P-2208-A-																			
-08-MI	41	6.5	0.08	2.54	0.12	0.58	0.41	0.18	1.22	<0.02	0.02	0.06	7.85	1.73	0.57	1.68	-18.48	-150.8	-3.0
-09-MI	63	6.6	0.07	4.09	0.04	0.38	0.40	0.10	2.96	<0.02	0.04	0.10	14.61	0.51	0.17	2.59	-16.79	-142.8	-8.5
-10-MI	67	6.6	0.06	4.94	0.04	0.40	0.34	0.09	3.26	<0.02	0.13	0.11	15.85	0.35	<0.15	2.75	-16.73	-142.1	-8.3
-11-MI	74	6.6	0.06	5.03	0.04	0.65	0.34	0.06	3.51	<0.02	0.10	0.10	17.43	0.23	<0.15	3.66	-16.79	-143.6	-9.2
-12-MI	57	6.9	0.07	2.45	0.05	0.35	0.44	0.05	3.53	<0.02	<0.02	0.11	12.50	0.18	<0.15	3.81	-16.90	-144.0	-8.8
-13-MI	54	6.8	0.07	1.49	0.05	0.38	0.41	0.05	4.31	<0.02	<0.02	0.11	12.21	0.20	<0.15	3.81	-17.10	-145.1	-8.3
-15-MI	108	6.6	0.14	3.60	0.17	1.60	2.18	0.38	5.04	0.03	<0.02	0.11	13.78	13.10	0.89	6.71	-22.81	-182.4	0.0
-16-MI	75	6.7	0.09	3.21	0.11	1.02	1.11	0.20	4.21	0.02	<0.02	0.10	13.27	5.17	0.79	4.88	-17.50	-145.4	-5.4
-17-MI	57	6.7	0.14	2.98	0.28	2.42	1.44	0.21	3.30	<0.02	0.02	0.07	6.12	6.51	0.30	6.86	-20.87	-162.8	4.8
-18-MI	42	6.8	0.06	0.89	0.04	0.40	0.39	0.05	2.88	<0.02	<0.02	0.11	8.69	0.62	0.16	3.05	-16.76	-142.7	-8.3
-19-MI	36	6.9	0.05	0.49	0.03	0.21	<0.1	0.04	2.98	<0.02	<0.02	0.10	7.86	0.20	<0.15	2.59	-16.69	-142.2	-8.3

Sample ID	EC	pH	Al	Ca	Fe	K	Mg	Mn	Na	Sr	Zn	F	Cl	SO_4	NO_3	HCO_3	$\delta^{18}O$	δD	d excess
	µS cm^{-1}		mg l^{-1}	mg l^{-1}	mg l^{-1}	mg l^{-1}	mg l^{-1}	mg l^{-1}	mg l^{-1}	mg l^{-1}	mg l^{-1}	mg l^{-1}	mg l^{-1}	mg l^{-1}	mg l^{-1}	mg l^{-1}	‰	‰	‰
-20-MI	61	6.5	0.16	3.30	0.28	3.55	1.70	0.25	1.73	<0.02	0.03	0.07	3.64	11.31	1.52	3.36	-23.19	-176.3	9.2
-21-MI	32	6.6	0.13	1.39	0.27	1.99	0.46	0.15	0.92	<0.02	0.02	0.07	4.14	1.26	0.31	3.51	-19.89	-151.9	7.3
-22-MI	24	6.8	0.07	0.98	0.09	0.60	0.19	0.08	0.81	<0.02	<0.02	0.09	3.46	1.55	0.30	1.98	-20.21	-157.3	4.4
-23-MI	81	6.8	0.07	1.19	0.07	0.81	1.21	0.07	7.18	<0.02	<0.02	0.13	19.13	0.94	<0.15	2.90	-16.91	-142.9	-7.6
-24-MI	47	6.9	0.08	0.83	0.07	0.23	0.51	0.07	4.10	<0.02	<0.02	0.09	10.46	0.47	0.21	1.37	-16.70	-143.0	-9.3
-25-MI	45	7.2	0.12	1.54	0.08	0.36	0.60	0.06	1.99	<0.02	<0.02	0.11	7.84	0.29	<0.15	4.42	-16.94	-143.9	-8.4
-26-MI	42	7.0	0.06	0.93	0.04	0.33	0.21	0.06	2.33	<0.02	<0.02	0.11	8.61	0.31	0.25	4.73	-17.22	-145.6	-7.8
-27-MI	90	6.9	0.11	1.77	0.11	0.64	1.18	0.08	6.99	<0.02	<0.02	0.11	19.48	0.40	0.27	8.69	-17.28	-145.7	-7.4
-28-MI	116	6.9	0.07	2.65	0.06	0.64	1.74	0.06	8.01	0.03	<0.02	0.12	25.24	0.82	0.48	12.81	-17.64	-148.7	-7.6
-29-MI	25	6.7	0.07	1.05	0.08	0.32	0.38	0.09	0.51	<0.02	<0.02	0.06	1.85	3.89	0.42	2.44	-21.02	-164.6	3.6
-30-MI	80	6.7	0.06	2.18	0.05	0.38	0.95	0.09	3.76	<0.02	<0.02	0.11	14.31	3.50	0.45	7.63	-17.55	-147.9	-7.5

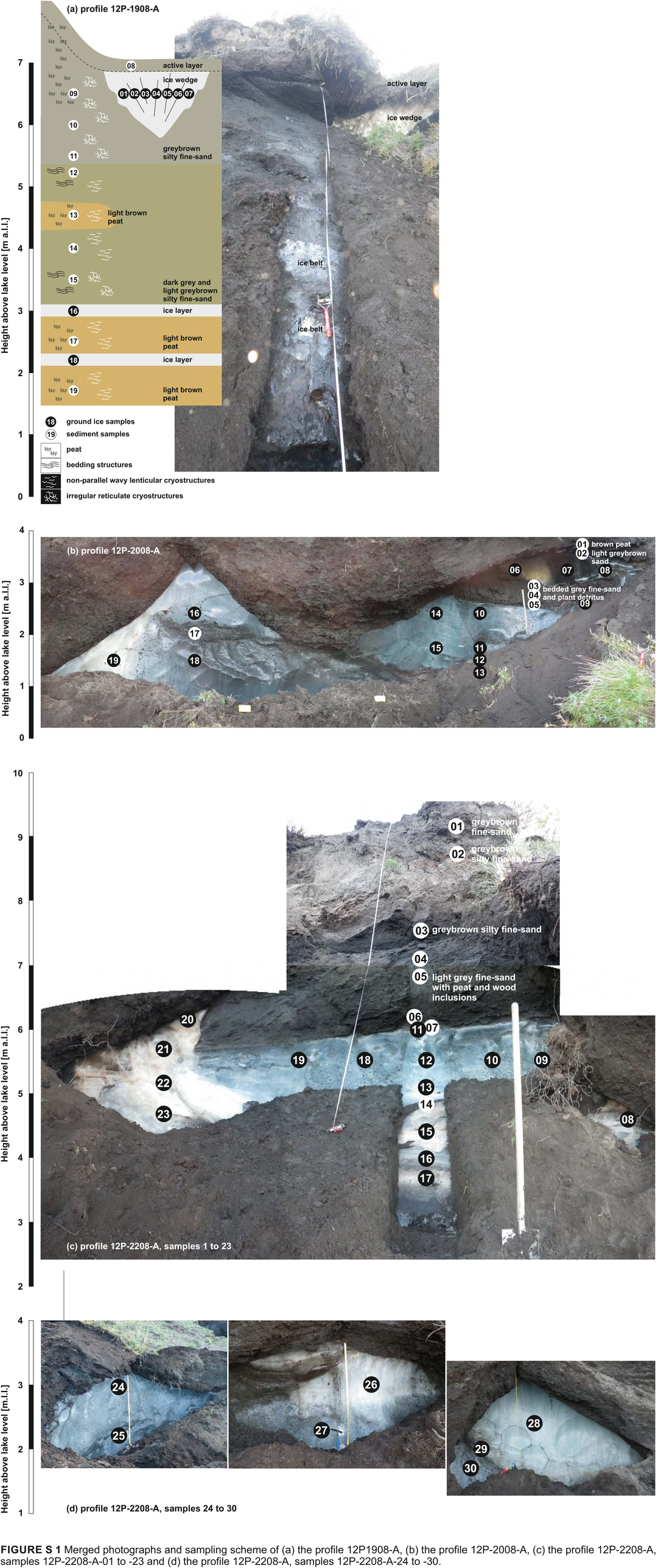

FIGURE S 1 Merged photographs and sampling scheme of (a) the profile 12P1908-A, (b) the profile 12P-2008-A, (c) the profile 12P-2208-A, samples 12P-2208-A-01 to -23 and (d) the profile 12P-2208-A, samples 12P-2208-A-24 to -30.

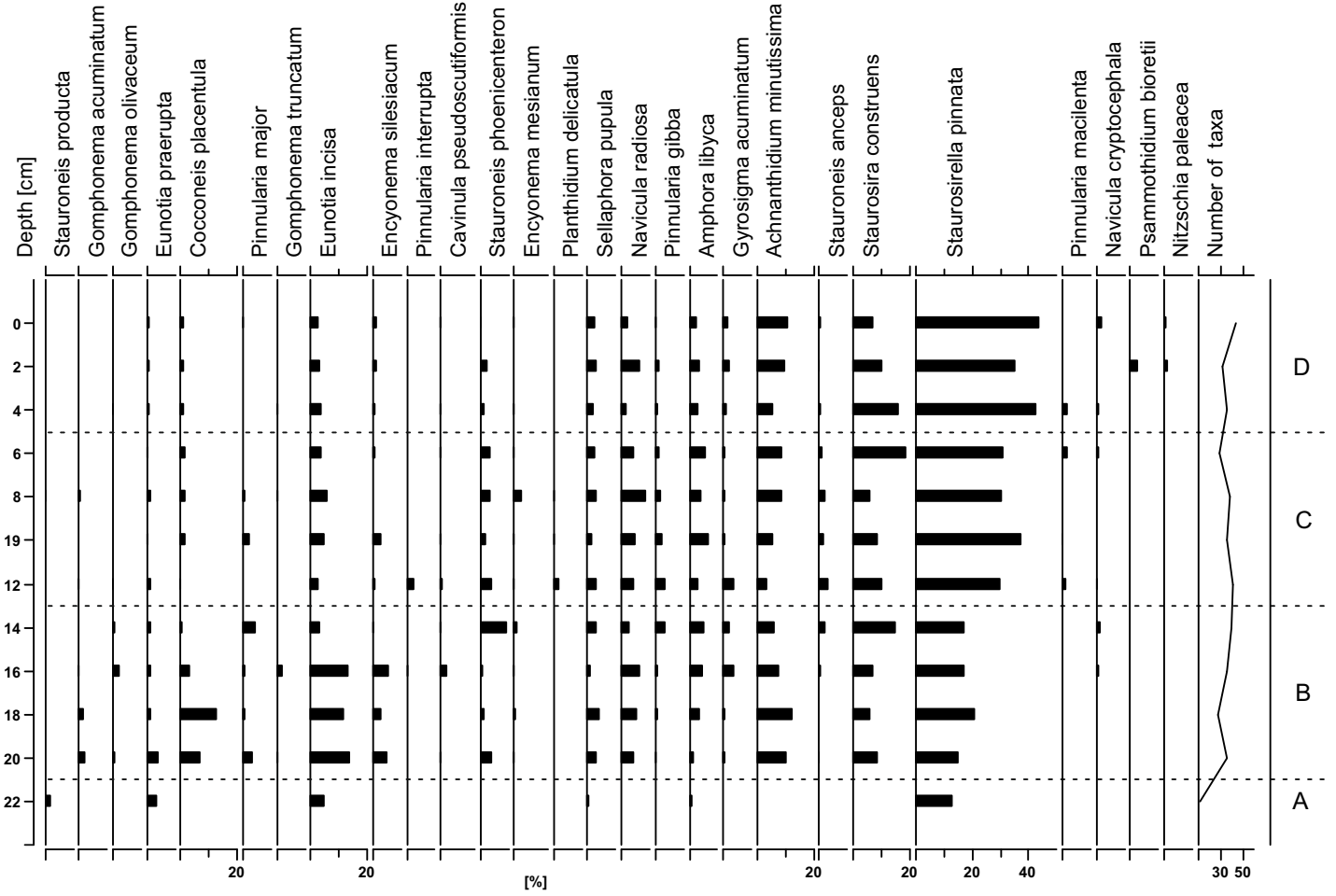

FIGURE S 2 Relative proportions of the most abundant diatom species (>2% abundance per sample) from short core 80-1 of modern lake sediments. The species are sorted by their weighted averaging scores from bottom left to upper right to highlight the major stratigraphic changes. Diatom species from short core of the modern lake sediments were divided into four zones. Within **zone A** (24-22 cm depth), 12 taxa were recorded. Dominants and subdominants of the zone were *Staurosirella pinnata, Eunotia incisa, Eunotia praerupta*. This zone is associated with a large share of valves of acidophilic and cold-water species.

Within **zone B** (22-14 cm depth), 52 taxa were identified. Along with the increase in species richness, increase the shares of the valves of species *Staurosirella pinnata*, *Eunotia incisa*, new dominants and subdomains appear - *Fragilaria construens*, *Achnanthidium minutissimum, Cocconeis placentula, Amphora libyca*, species of genus *Encyonema*, living on submerged aquatic plants - *Encyonema silesiacum*, *Encyonema mesianum*. All this reflects the processes of temperature rise in the environment, lengthening of the growing season and the minerogenic inflow from the catchment area.

Zone C (14-6 cm depth) species richness is 62 species. To small sized, dominant species are added benthic alkaliphilic large sized slowly growing species as *Gyrosigma acuminatum*. All these indicates a further increasing in air temperature, the turbulence and mineralization of water and decreasing in the water level in the reservoir.

Zone D (6-0 cm depth) also represented by 62 species. Benthic, alkaliphilic, cosmopolitan species predominate. The zone has the highest percentage of valves of *Staurosirella pinnata.* All this indirectly reflects an increasing in air temperature, and the period of open water.

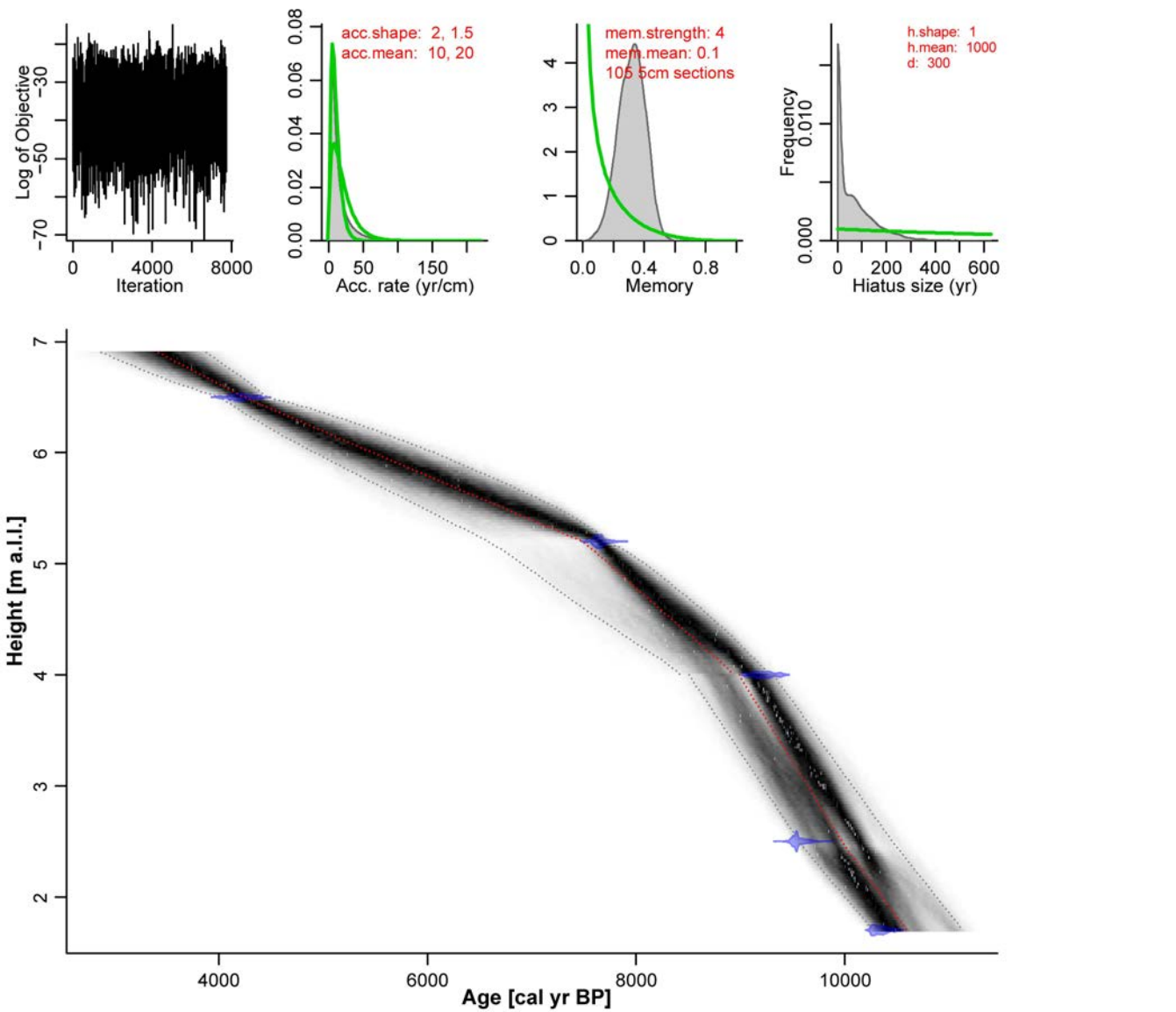

FIGURE S 3 Age-depth model for profile 12P-1908-A. The age-depth model was calculated using Bacon 2.2 modelling routines (Blaauw and Christen 2011) from five AMS 14C dates and calibrated with the IntCal13 calibration curve (Reimer et al. 2013). The red dotted line indicates median ages modelled for each centimetre along the core. Calibrated dates are shown as transparent blue violin plots. Grey stippled lines illustrate 95% confidence intervals of the modelled age-depth relationship. The three upper graphs describe the quality of Markov Chain Monte Carlo iterations the model produced. The left graph shows the variance between iterations. The middle and right graphs show prior (green lines) and posterior (grey histograms) density functions for accumulation rate and memory.

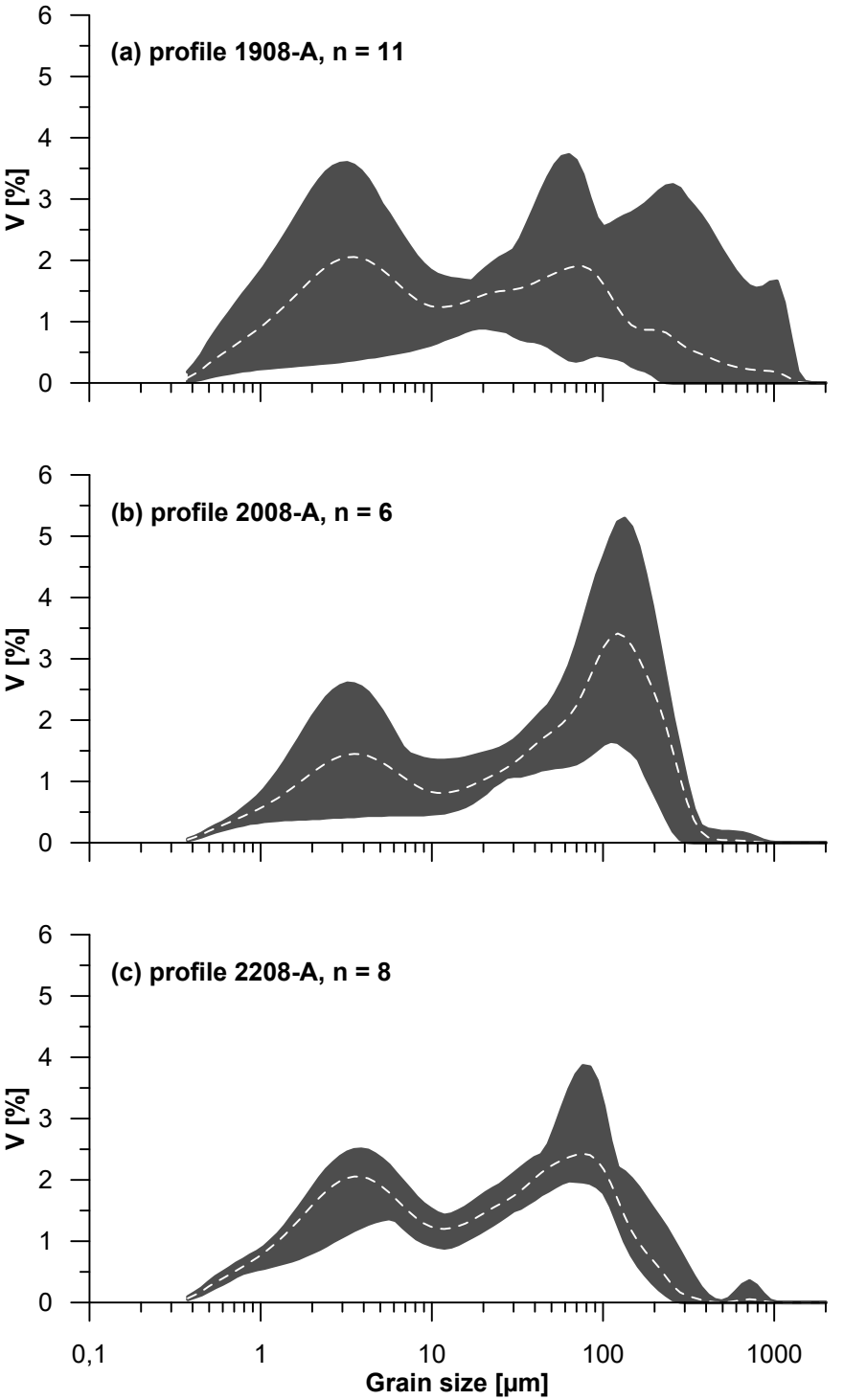

FIGURE S 4 Grain-size distribution curves of the three studied profiles (a) 12P-1908-A, (b) 12P-2008-A and (c) 12P-2208-A. White dotted curves shown mean grain-size values and grey shaded area shows minima and maxima values.

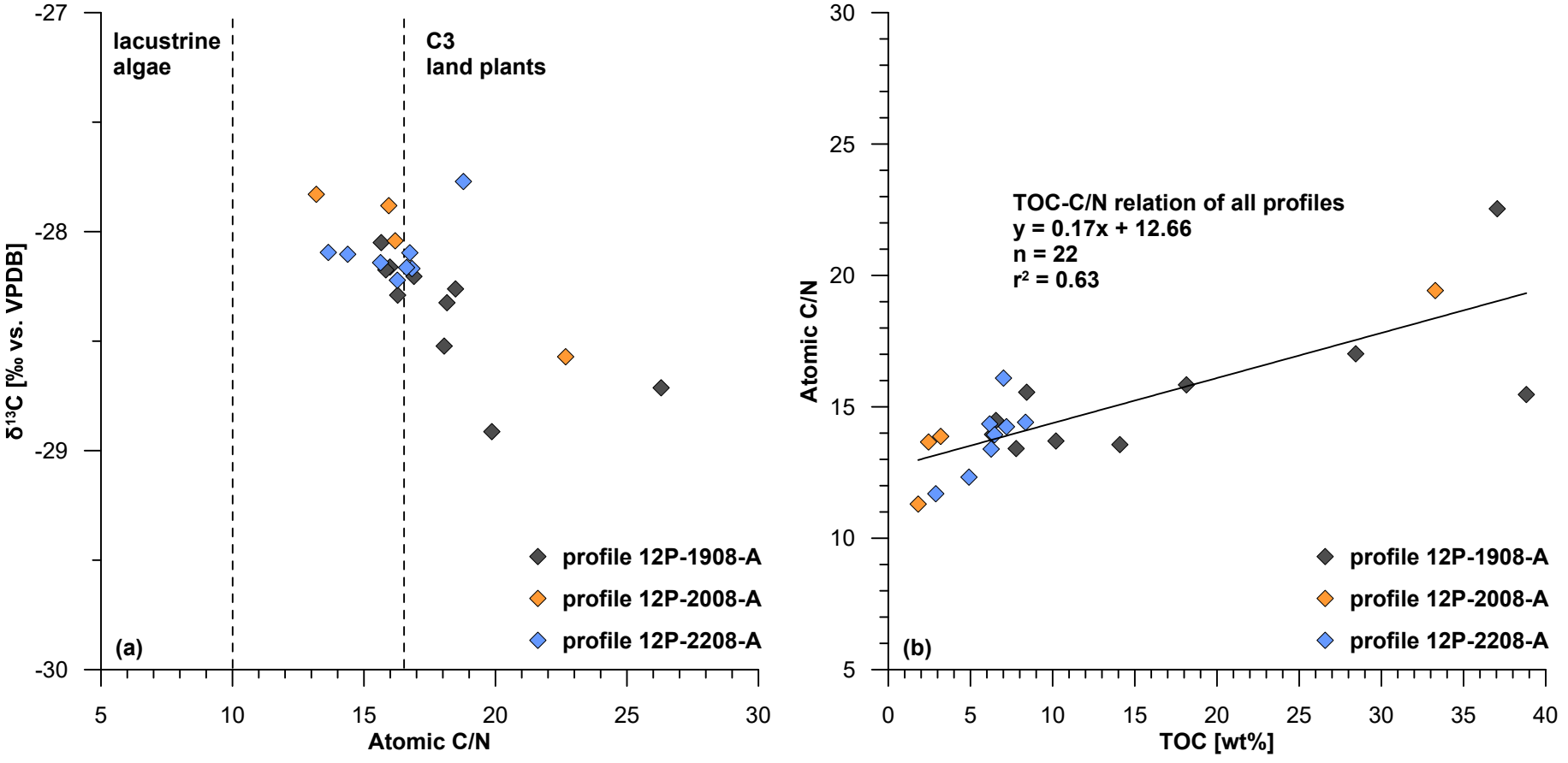

FIGURE S 5 Organic matter characteristics of sediment samples from the Shirokovsky Kholm Pingo showing (a) the distribution of the C/N ratio – $\delta^{13}C$ of TOC relationship according to Meyers (1997) and (b) the correlation of TOC and C/N.

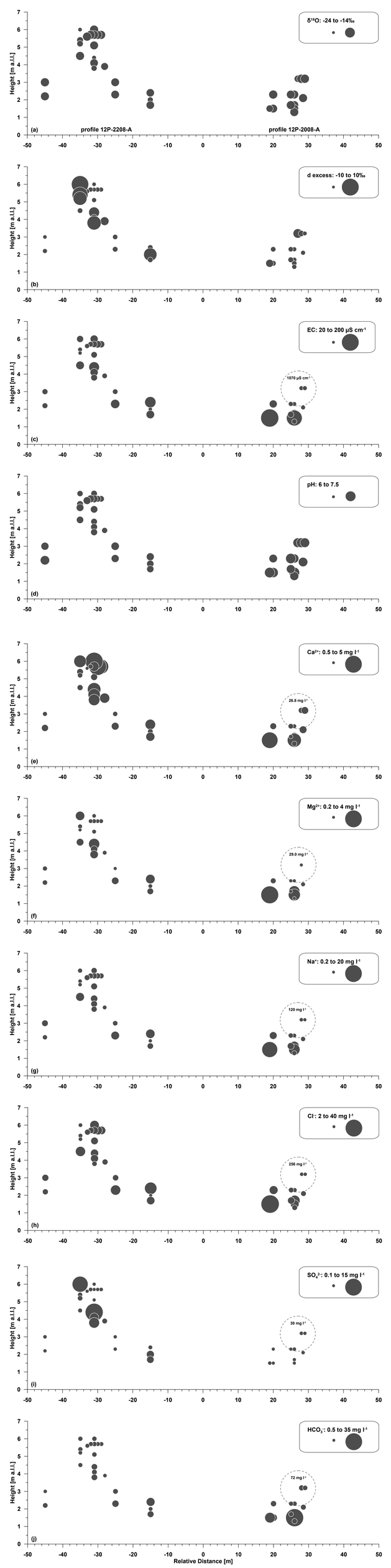

FIGURE S 6 Composition of massive ice samples: (a) $\delta^{18}O$, (b) d excess, (c) electrical conductivity – EC, (d) pH, (e-g) major cations and (h-i) major anions from profiles 12P-2008-A and 12P-2208-A. Exceptional high EC of one sample (12P-2008-A-06-PI) in profile 12P-2008-A is given as dotted circle not to scale.

FIGURE S 7 Micropalaeontological proxy data from profile 12P-1908-A of (a) relative proportions of pollen and non-pollen palynomorphs, (b) testaceans in ecological groups as present-absent information, (c) relative proportions of the most abundant diatom species (>2% abundance per sample) and (d) relative proportions of the most abundant chironomid taxa. The diatom species (c) and the chironomid taxa (d) are sorted by their weighted averaging scores from bottom left to upper right to highlight the major stratigraphic changes.

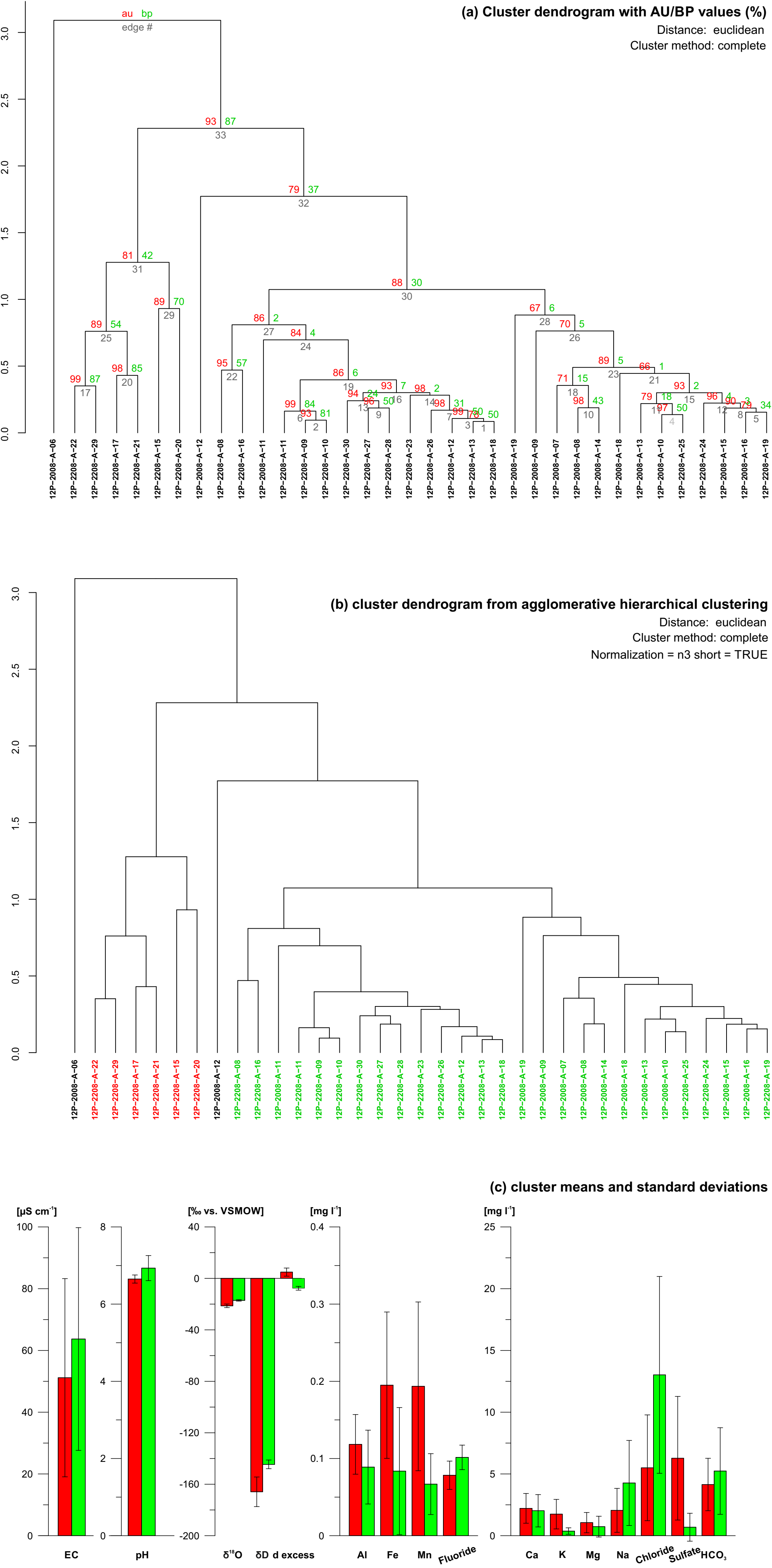

FIGURE S 8 Results of the cluster analysis given as (a) cluster dendrogram from agglomerative hierarchical clustering with “complete” as clustering method. Grey numbers refer to the dendrogram edges, red and green numbers refer to approximately unbiased p-values (AU, in red) and bootstrap probability values (BP, in green) from the significance analysis (Suzuki and Shimodaira 2015), which supplies probabilities for each edge in the cluster dendrogram, (b) cluster dendrogram from agglomerative hierarchical clustering with “complete” as clustering method. Colour coding refers to the clusters in which the samples were sorted (two clusters and two additional samples) and (c) cluster means (coloured bars) and standard deviation (error bars) of EC, pH, anions, cations, stable isotope signature according to the clusters shown in Figure S 8b.